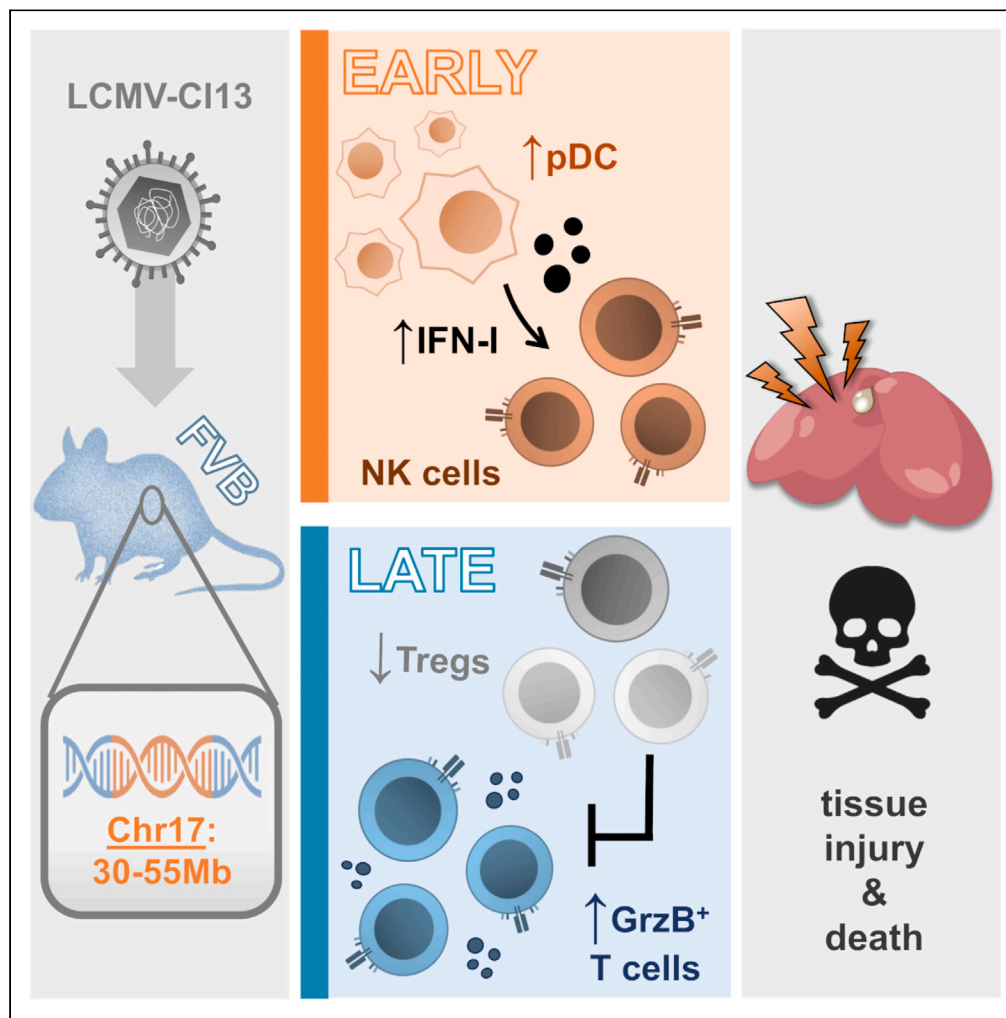


Article

Mice with FVB-derived sequence on chromosome 17 succumb to disseminated virus infection due to aberrant NK cell and T cell responses



Taylor N. Tibbs,
Lauren J.
Donoghue, Ashlyn
A. Buzzelli, ...,
Martin T. Ferris,
Samir N.P. Kelada,
Jason K. Whitmire

jwhitmire@email.unc.edu

Highlights

25Mb locus on FVB
Chromosome 17 confers
lethal susceptibility to
LCMV-Clone13

NK cells contribute to early
liver damage and platelet
loss

T cells contribute to late
liver damage, platelet loss,
and death

FVB-Chr17 tracks with
cytotoxic CD4 T cells and a
loss of Tregs

Tibbs et al., iScience 26, 108348
November 17, 2023 © 2023 The
Author(s).
[https://doi.org/10.1016/
j.isci.2023.108348](https://doi.org/10.1016/j.isci.2023.108348)



Article

Mice with FVB-derived sequence on chromosome 17 succumb to disseminated virus infection due to aberrant NK cell and T cell responses

Taylor N. Tibbs,¹ Lauren J. Donoghue,² Ashlyn A. Buzzelli,² Ichiro Misumi,² Maggie DeMonia,² Martin T. Ferris,² Samir N.P. Kelada,² and Jason K. Whitmire^{1,2,3,4,*}

SUMMARY

Zoonotic arenavirus infections can result in viral hemorrhagic disease, characterized by platelet loss, petechia, and multi-organ injury. The mechanisms governing these outcomes are likely impacted by virus strain and infection dose, as well as an individual's genetic background and immune constitution. To better understand the processes leading to severe pathogenesis, we compared two strains of inbred mice, C57BL/6J (B6) and FVB/NJ (FVB), that have diametrically opposed outcomes during disseminated lymphocytic choriomeningitis virus (LCMV) infection. Infection caused minimal pathogenesis in B6 mice, whereas FVB mice developed acute hepatitis and perished due, in part, to aberrant NK cell and T cell responses. Susceptible mice showed an outgrowth of cytolytic CD4⁺ T cells and loss of Treg cells. B6 congenic mice with the FVB allele at a 25Mb locus on chromosome 17 recapitulated FVB pathogenesis upon infection. A locus containing a limited number of variants in immune-related genes greatly impacts survival during infection.

INTRODUCTION

Arenaviruses can cause severe viral hemorrhagic disease and mortality.¹ Lassa fever virus, a rodent-borne arenavirus endemic in Africa, infects approximately 500,000 people and causes 5,000–10,000 deaths annually.^{2,3} Other arenaviruses such as Junin, Machupo, and Sabia cause smaller outbreaks, but have mortality rates between 10 and 50%.^{1,4} Clinical manifestations of arenavirus-associated hemorrhagic disease include thrombocytopenia, petechia, disseminated intravascular coagulation, and tissue hemorrhage, which can be lethal if left untreated.

Few animal models mimic human hemorrhagic disease. Viral hemorrhagic disease can be recapitulated in non-human primates,^{4,5} but these models are expensive and often require high biosafety level containment (BSL3/4). Reproducing hemorrhagic disease in non-primate animals is often complex, involving immunocompromised hosts, modified/attenuated virus, or require species for which there are limited reagents. Lymphocytic choriomeningitis virus (LCMV) is an arenavirus that naturally infects and persists in mice in the wild. Despite not being a zoonotic infection, LCMV infections of laboratory mice can be used to understand elements of the host response that contribute to pathogenesis. The LCMV mouse model is well-established and experiments with LCMV can be performed at lower levels of bio-containment with an abundance of tools for mice. LCMV-Clone 13 (Cl13) establishes a systemic and chronic infection in adult mice marked by eventual T cell exhaustion.⁶ Inbred C57BL/6J (B6) mice infected with Cl13 develop transient disease symptoms (weight and temperature loss), but largely recover within 2 weeks. In contrast, FVB/N (FVB) mice develop a severe hemorrhagic-like disease that is fatal within 5–10 days post-infection.^{7,8} The genetic basis for these divergent outcomes is unknown; identifying the causal genetic factors for these responses will increase our understanding of how pathogenesis unfolds during infection.

Here we show that pathogenesis in FVB mice mirrors the clinical symptoms of viral hemorrhagic fever in humans, and susceptibility is associated with a specific genetic locus on chromosome 17. Cl13-infected FVB mice develop hallmark features of viral hemorrhagic disease as observed in humans, including thrombocytopenia, hepatitis, and splenic necrosis. Cl13-mediated pathology in FVB mice is driven by both natural killer (NK) cells, which illicit early liver damage, and T cells, including an outgrowth of cytolytic CD4⁺ T cells and a precipitous loss of regulatory T cells, which drive lethality a few days later. Using forward genetics and quantitative trait locus mapping (QTL), we identify a susceptibility locus located in an immune-dense region of mouse chromosome 17. B6 congenic mice with the FVB allele at this locus exhibited severe pathogenesis including excessive interferon production and aberrant innate and adaptive immune responses.

¹Department of Microbiology and Immunology, UNC-Chapel Hill School of Medicine, Chapel Hill, NC 27599, USA

²Department of Genetics, UNC-Chapel Hill School of Medicine, Chapel Hill, NC 27599, USA

³Lineberger Comprehensive Cancer Center, UNC-Chapel Hill School of Medicine, Chapel Hill, NC 27599, USA

⁴Lead contact

*Correspondence: jwhitmir@email.unc.edu

<https://doi.org/10.1016/j.isci.2023.108348>



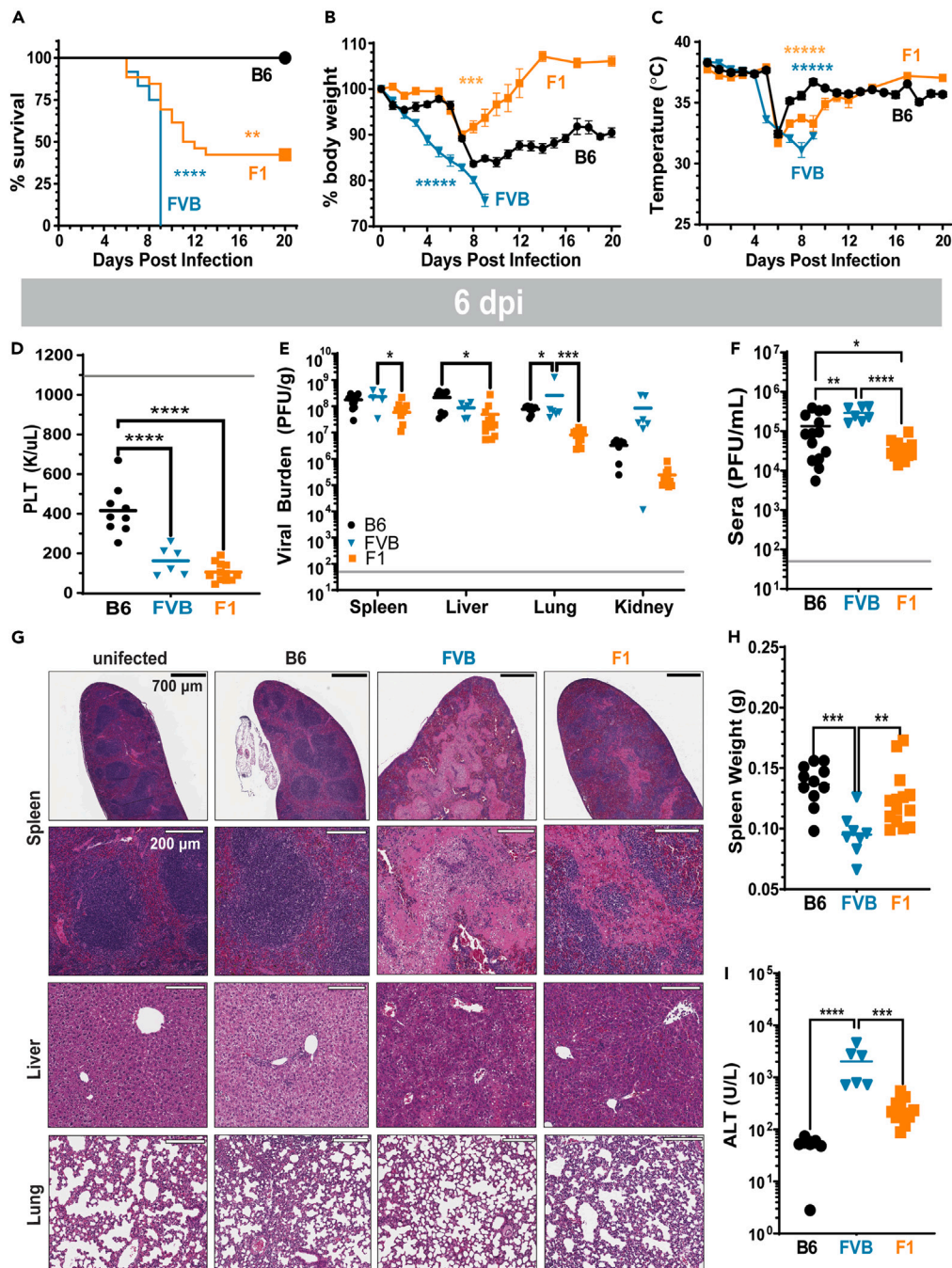


Figure 1. FVB:Cl13 pathogenesis is heritable and affects multiple organs

FVB, B6, and F1 (B6xFVB) mice were challenged with LCMV-Clone13 and monitored for physical signs of illness across time or assessed at day 6 post-infection for viral burden, liver histology, and blood Alanine Aminotransferase (ALT) activity.

(A) The frequency of survival across time.

(B) Body weight changes across time, including for mice surviving from day 8 onwards.

(C) Body temperature changes based on rectal measurements, including for mice surviving past day 8. (D-I) Cohorts of infected mice were necropsied at day 6 post-infection.

(D) Platelet counts as determined by complete blood cell count. Average levels in uninfected mice represented by horizontal gray line.

(E) Viral burden in tissues based on plaque assay. Horizontal gray line marks the limit of detection.

(F) Viral burden in sera.

(G) H&E stains of spleen, liver, and lung sections. Black scale bar = 700 μ m, white bar = 200 μ m.

Figure 1. Continued

(H) Whole spleen weight.

(I) Alanine aminotransferase activity in sera. Results are combined from multiple experiments with 6–25 mix-sex mice per group per timepoint. Horizontal bars represent mean (D–F, H and I). Data are represented as mean \pm SEM (B and C). Statistical analyses included Kaplan-Meier (A) and unpaired one-way ANOVA (B–F, H and I) (* $p < 0.05$, ** $p < 0.01$, *** $p < 0.001$, **** $p < 0.0001$). The Grub's outlier test was used to identify outliers in panel (H) and one data point was excluded (significant outlier, $p < 0.05$).

RESULTS**FVB mice develop a severe hemorrhagic disease post-CI13 infection that follows a semidominant inheritance pattern**

Previous studies have shown that the FVB strain of mice rapidly succumbs to infection with CI13.^{7,8} Consistent with those reports, we observed that FVB, but not B6 mice, perish within 10 days of infection (Figure 1A). Prior to euthanasia, the FVB mice showed a precipitous loss of body weight and temperature (Figures 1B and 1C), as well as other physical signs of illness, including petechia and mucosal hemorrhage by day 6 of infection. While B6 mice had a significant loss of weight from day 6 to day 8, they gradually regained body weight. The B6 mice showed a prominent drop in body temperature at day 6, but this was followed by a partial recovery, though the mice remained slightly hypothermic ($\sim 36^\circ\text{C}$) through day 20 post-infection.

FVB and B6 mice were intercrossed to produce B6FVBF1 (F1) progeny. Following infection, 50% of the F1 mice required euthanasia, indicating a semi-dominant inheritance of susceptibility (Figure 1A). The F1 mice varied in susceptibility according to sex: all males succumbed to infection, whereas only 25% of females perished (Figure S1A). F1 mice from reciprocal crosses (FVB \times B6F1 and B6 \times FVBF1) exhibited similar phenotypes, indicating that susceptibility to infection did not depend upon the direction of the F1 cross with respect to dam genotype (Figures S1B–S1D). B6FVBF1 mice were used in all further experiments.

F1 mice were similar to B6 mice with regard to weight loss kinetics during the first week of infection. Interestingly, F1 mice surviving past day 8 rapidly recovered weight to an extent that was more robust than B6 mice (Figure 1B). The infected F1 mice resembled B6 mice in the loss and recovery of body temperature over the course of infection.

To better understand the pathogenic process in these mice, cohorts of B6, FVB, and F1 mice were examined at day 6 post-infection, prior to when mice showed mortality. There was a significant loss of circulating platelets in FVB and F1 mice compared to B6 (Figure 1D). Viral burdens in the lung, kidney, and sera were higher in FVB mice compared to B6, while burdens in the spleen and liver were comparable (Figures 1E and 1F). In contrast, the viral burden across all F1 tissues was lower than B6 or FVB mice. Though viral titer in the kidney varied between groups, we observed no differences in creatinine levels (Figure S1E). The amount of virus in the tissues of each cohort did not track with outcome, implying that susceptibility to infection is controlled by host genetic factors other than direct, virus-induced tissue injury.

Compared to tissues in B6 mice at day 6 post-infection, the spleens of FVB mice showed more tissue necrosis, degradation of normal splenic architecture, and cellular loss predominantly within the marginal zone, a dominant region for CI13 infection^{9–11} (Figure 1G). There was a significant loss of spleen weight (Figure 1H) and cell counts in the FVB mice (Figures S1F). The livers of FVB mice had prominent necrotic lesions, apoptotic bodies, destroyed vessel linings, and fatty degeneration (Figure 1G) and, consistent with this liver injury, the sera of FVB mice contained elevated alanine aminotransferase (ALT) activity (Figure 1I). The F1 mice displayed intermediate amounts of splenic and liver injury and ALT activity in sera (Figures 1G–1I). Lung injury in infected FVB, F1, and B6 mice appeared comparable at 6 days post-infection (dpi) (Figure 1G), suggesting that the FVB genetic background primarily affects the liver and spleen during infection. This contrasts with other CI13-susceptible strains of mice, such as PL/J and NZB,¹² that show substantial lung edema and lower amounts of liver injury (compared to FVB).^{7,8,13} Among FVB mice that did not perish until days 8–10, there was a moderate increase in lung edema and tissue damage compared to B6 mice, suggesting that lung pathogenesis predominantly occurs during the late stages of disease in moribund FVB mice (Figure S1G). In sum, we confirm that the FVB genetic background confers susceptibility to CI13 infection,^{7,8} primarily driving pathogenesis in the spleen and liver.

Pathogenesis in FVB mice is evident in the spleen and liver early during CI13 infection

The severe level of tissue damage at 6 dpi within the spleens and livers of FVB mice prompted us to examine earlier stages of infection to determine when pathogenesis begins. Since the outcome of CI13-infected F1 female mice varied from mouse-to-mouse, we focused our efforts on F1 males. We found that FVB mice show signs of hemorrhagic disease as early as 2–3 days post-infection. Viral burden in the spleen and liver was largely comparable between B6, FVB, and F1 mice during early stages of infection (Figure 2A) with a statistically significant increase in the spleen of F1 mice compared to B6 at day 2. Elevated ALT activity in sera was biphasic (Figure 2B), with one peak at 48 h post-infection and another prominent peak at day 6. The ALT peak at 48 h suggests that early liver damage might be driven by an innate immune response in FVB mice. On day 3 of infection, FVB livers showed early-stage edema, immune infiltrates, and fatty degeneration (Figure 2C), and FVB spleens displayed immune foci and early necrotic lesions within white pulp regions (Figure 2D). Cleaved caspase-3 staining revealed increased apoptosis in FVB mice as early as 3 dpi within the spleen and in both spleen and liver at 6 dpi, compared to B6 mice (Figures 2E and 2F). These findings in FVB mice implicate innate immune mechanisms driving pathogenesis in the spleen and liver.

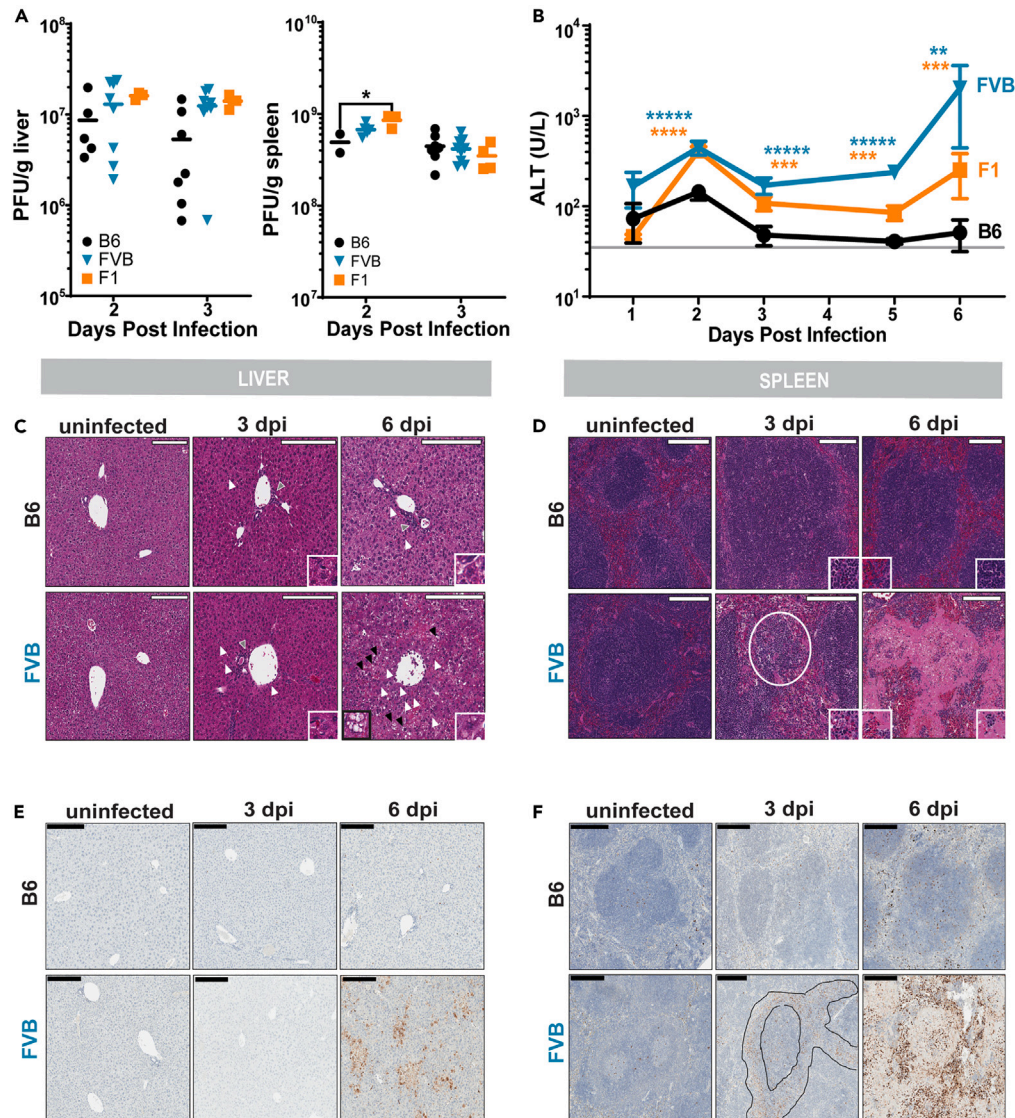


Figure 2. Spleen and liver damage in FVB mice begins early during CI13 infection

Mixed sex B6 and FVB mice and male F1 mice were infected with LCMV-CI13 and evaluated 0, 2, 3, 5, and 6-day post infection for viral burden, blood ALT activity, spleen and liver histology and cleaved-caspase-3 immunohistochemistry.

(A) Viral burden in spleen and liver at 2 and 3 dpi. Two to eight mice per group.

(B) Daily alanine aminotransferase activity in sera. Three to twelve mice per strain per time point.

(C) H&E liver histology at 0, 3, and 6 dpi. Black arrows highlight examples of fatty degeneration, with zoomed-in examples in black insets. White arrows represent examples of apoptotic bodies, with zoomed-in examples in white insets.

(D) H&E spleen histology 0, 3, and 6 dpi. White circled area highlights early lesion formation. Examples of the varying cellular composition in zoomed-in insets.

(E) Cleaved caspase-3 staining of livers at 0, 3, and 6 dpi.

(F) Cleaved caspase-3 staining of spleens 0, 3, and 6 dpi. Black outline marks concentrated areas of staining within marginal zone. All scale bars are 200 μ m.

Horizontal bars represent mean (A). Data are represented as mean \pm SEM (B). Data are pooled from multiple independent experiments. Statistical analysis used unpaired one-way ANOVA (A and B) (* $p < 0.05$, ** $p < 0.01$, *** $p < 0.001$, **** $p < 0.0001$).

FVB mice have more Nkp46⁺ NK cells than B6 before and after CI13 infection

Previous studies observed that LCMV-infected FVB mice rapidly make type-1 interferon (IFN-I) at levels significantly higher than in infected B6 mice.⁸ Concordant with this finding, prior to infection FVB mice had more splenic plasmacytoid dendritic cells (pDCs), key producers of IFN-I during viral infection,¹⁴ than B6 mice (Figure S2A). IFNs activate NK cells to become cytolytic during virus infections^{15,16} and promote robust T cell responses to LCMV.^{14,17,18} Prior to infection, FVB mice had a larger NK cell (CD3⁺DX5⁺Nkp46⁺) population than B6 mice (Figure S2B).

NK cells in uninfected FVB mice also expressed more of the activation marker Nkp46 per cell than B6 mice (Figure S2C), suggesting that FVB NK cells are poised to react to inflammatory stimuli.

The CD8⁺ T cell response to infection in B6 and FVB mice differs in robustness

T cells typically protect against LCMV, but when the infection has disseminated widely, T cells can cause fatal collateral damage while eliminating virus-infected cells in vital tissues. We quantified T cell responses at baseline and 6 days after infection, before the FVB mice became moribund. FVB mice had a lower frequency of splenic CD8⁺ T cells compared to B6 mice before infection (Figure S2D), though the number of CD8⁺ T cells at baseline was similar (data not shown). Following infection, the spleens of FVB mice had fewer activated CD8⁺ T cells compared to B6, though numbers were similar in the liver (Figures 3A and 3B). The number of activated CD8⁺ T cells in the spleens and livers of F1 mice was similar or greater than in B6 mice, suggesting the size of the CD8⁺ T cell response alone does not determine fatality.

Effector CD8⁺ T cells express and degranulate granzyme B (GrzB) to kill infected target cells. We observed fewer splenic GrzB⁺ CD8⁺ T cells in FVB mice compared to B6 mice, whereas F1 mice showed elevated numbers of these cells in the spleen and liver (Figures 3C and 3D). Moreover, splenic CD8⁺ T cells from FVB mice exhibited enhanced degranulation following TCR or peptide stimulation, though the opposite was observed in the liver (Figures 3E and 3F). Our data show that the strength of the CD8⁺ T cell response in CI13-infected FVB and F1 mice differs by tissue, but does not track with survival, suggesting pathogenic mechanisms beyond CD8⁺ T cells.

CI13-infected FVB mice show an outgrowth of GrzB⁺ CD4⁺ T cells and a precipitous loss of Treg cells

At baseline, uninfected FVB mice had both a higher frequency and 3.5-fold more CD4⁺ T cells compared to age/sex-matched B6 mice (Figure S2D and data not shown). By 6 days of infection, B6, FVB, and F1 mice had similar numbers of activated CD4⁺ T cells in the spleen, but FVB and F1 mice had significantly elevated numbers of activated CD4⁺ T cells in the liver (Figures 4A and 4B). B6 mice mainly generate Th1 or Tfh subsets during infection and GrzB⁺ CD4⁺ represent a minor population; however, the CD4⁺ T cells in FVB and F1 mice were highly enriched for a GrzB⁺ subset (Figures 4C and 4D). The FVB and F1 CD4⁺ T cells expressed significantly more GrzB on a per cell level than did the GrzB⁺ B6 CD4⁺ T cells (data not shown). CD4⁺ T cells from the spleen and liver in FVB mice showed enhanced degranulation upon TCR triggering (Figures 4E and 4F), as well as higher gMFI of surface CD107a and CD107b compared to cells from B6 mice (data not shown), suggesting that FVB CD4⁺ T cells are more set to degranulate. Many FVB CD4⁺ T cells expressed significantly more of the liver-homing chemokine receptor CXCR6 than B6 CD4⁺ T cells (Figures S3A and S3B), which may explain why FVB mice have more CD4⁺ T cells in the liver (Figure 4B). There were lower frequencies of Th1 (Tbet⁺) cells in naive and CI13-infected FVB livers compared to B6 livers and little difference in the spleen (Figures S3C and S3D). There were no differences in Th2 or Tfh cell populations (data not shown). The frequency of CD4⁺ Foxp3⁺ Tregs prior to infection was lower in the spleens of FVB mice, and after infection there was a striking loss of Treg cells in the spleens and livers of FVB mice compared to B6 (Figures 4G and 4H). In sum, infected FVB mice show an increase in cytotoxic CD4⁺ T cells and a loss of T regulatory (Treg) cells.

CD4⁺ and CD8⁺ T cells contribute to lethality in FVB mice

To examine whether T cells contribute to pathogenesis in LCMV-infected FVB mice, cohorts of FVB mice were given non-depleting isotype antibody or depleting antibody against CD8⁺ or CD4⁺ T cells. As expected, all FVB mice that were given a non-depleting antibody required euthanasia following CI13 infection (Figure 5A). There was a significant improvement in survival among FVB mice depleted of CD4⁺ or CD8⁺ T cells. Surprisingly, CD4⁺ T cell depletion had the most profound impact on survival and platelet recovery (Figures 5A and 5C). Removing CD4⁺ or CD8⁺ T cells lowered serum ALT activity at day 6 dpi, with CD8 depletion reaching significance (Figure 5B). At day 6, the spleens and livers from CD4- and CD8-depleted FVB mice showed less tissue damage compared to T cell-replete mice (Figure 5D). These data indicate that late-stage pathogenesis and lethality involves both CD4⁺ and CD8⁺ T cells, with each likely playing distinct roles.

Differential CI13 susceptibility between B6 and FVB mice is associated with a quantitative trait locus on chromosome 17

The significant strain differences in CI13 susceptibility between inbred B6 and FVB mice indicate that genetic variation influences disease pathogenesis and mortality. To identify specific genetic factors driving these differences in susceptibility, we designed a forward genetic breeding scheme by which we backcrossed F1 sires to B6 dams, generating B6FVBN2 (N2) mice (Figure 6A). As was the case with F1 mice, N2 mice displayed an intermediate phenotype of CI13 lethality (42.3% survival) (Figure 6B). Sex effects on susceptibility were still apparent, but less distinguished in survivorship between N2 males and females (31.25% survival males, 50% survival females) (Figure S4A). Quantitative trait locus (QTL) mapping of death by 8 dpi in 63 N2 mice revealed a genome-wide significant QTL on chromosome 17 (Chr17:30-55 Mb), explaining 24% of variance in susceptibility (Figures S4B). N2 mice that had the FVB-Chr17 QTL allele were three times more likely to perish after CI13 infection (Figure 6C).

Using Ensembl Variant Effect Predictor (VEP)¹⁹ along the Chr17:30-55Mb interval, we identified 242 missense coding variants in the FVB allele with putative deleterious effects on protein structure and function (Figure 6D). These effects were further confirmed with Sorting Intolerant From Tolerant (SIFT) analysis²⁰ (Table S1). Among genes with immune-related functions or functions that may impact immune cells outside of the major histocompatibility complex (MHC), four (*Ubash3a*, *Umodl1*, *Cyp4f13*, and *Runx2*) contained at least one missense variant predicted to be deleterious. *Ubash3a* is a negative regulator of TCR-CD3 T cell activation and function, and the FVB variant falls within a post-translational regulatory region.^{21–23} *Runx2* influences a variety of functions in both bone development and in immune cell responses,

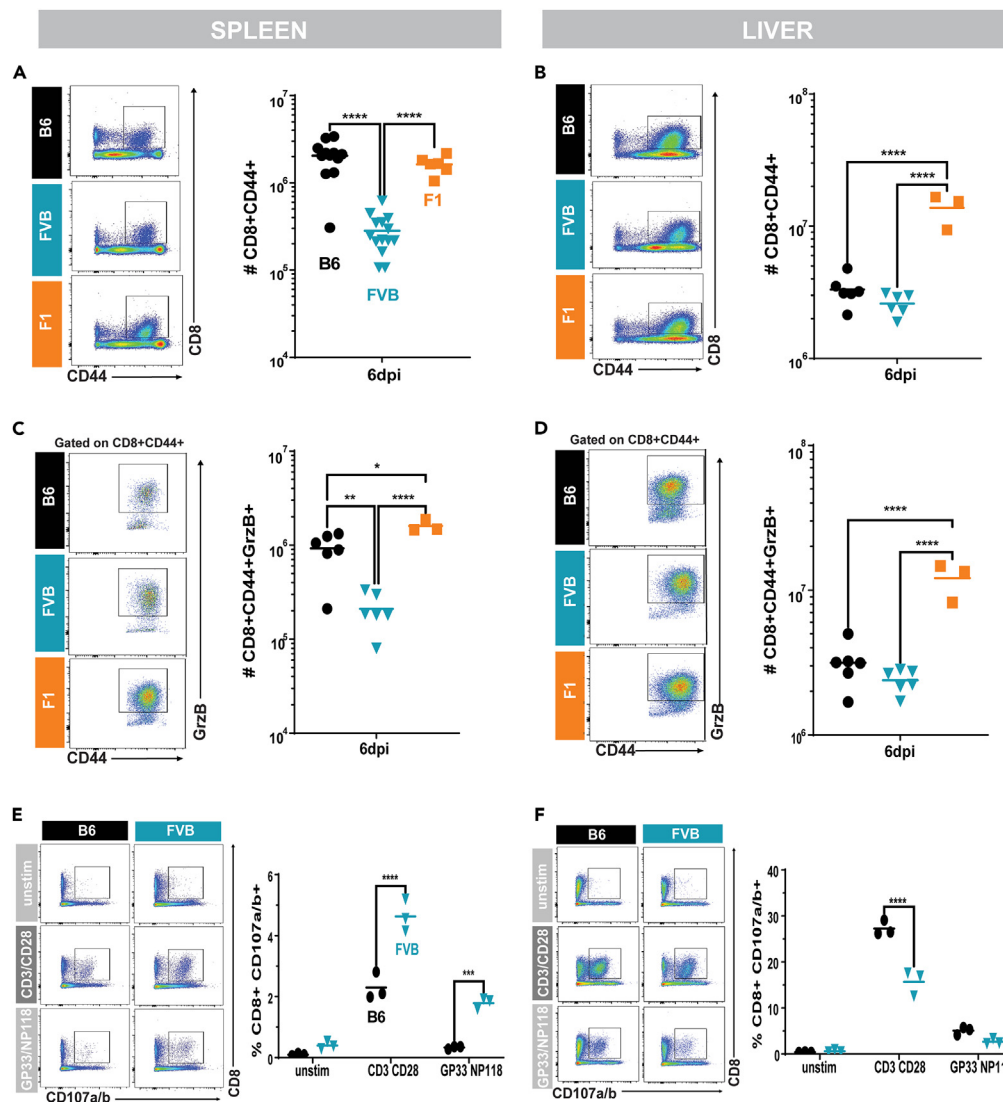


Figure 3. CD8⁺ T cell populations vary by tissue in C113-infected FVB mice

B6, FVB, and F1 mice were challenged with LCMV-C113. At day 6 post-infection, spleen and liver cells were isolated and CD8⁺ T cells were analyzed by flow cytometry.

(A) Representative flow plots and total cell count of CD8⁺CD44⁺ cells in spleen.

(B) Representative flow plots and total cell count of CD8⁺CD44⁺ cells in liver.

(C) Representative flow plots and total cell count of CD8⁺CD44⁺GrzB⁺ cells in spleen.

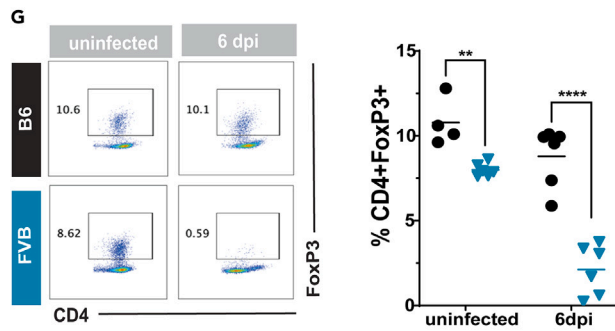
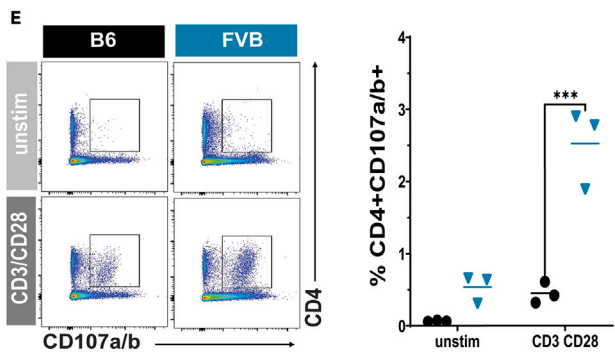
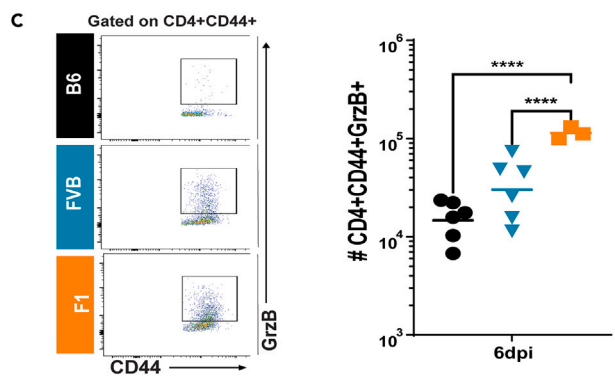
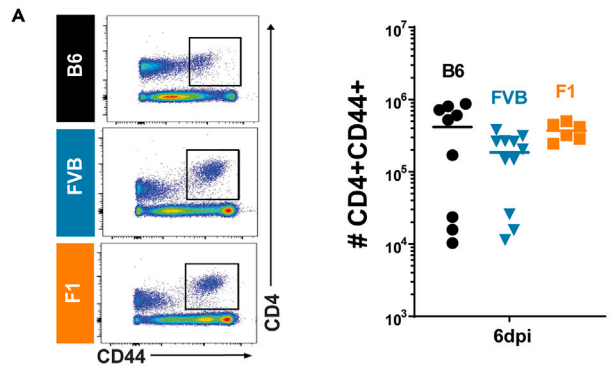
(D) Representative flow plots and total cell count of CD8⁺CD44⁺GrzB⁺ cells in liver.

(E and F) Single cell leukocyte preparations from the spleens and livers of B6 and FVB mice were stimulated *ex vivo* with anti-CD3/CD28, GP₃₃/NP₁₁₈ peptides, or were left unstimulated. Samples then stained for surface CD107a and CD107b and analyzed by flow cytometry. (E) Representative flow plots and total frequency of CD107a/b⁺CD8⁺ T cells from spleen. (F) Representative flow plots and total frequency of CD107a/b⁺CD8⁺ T cells from liver. Combined results of multiple independent experiments with 3–14 mice per group; all F1 mice were male, B6 and FVB mice were mixed sex. All flow cytometry data were gated on viability dye-negative, singlet cells. Horizontal bars represent mean. Statistical analysis used unpaired one-way ANOVA (A–D) and student's t-tests (E and F) (*p < 0.05, **p < 0.01, ***p < 0.001, ****p < 0.0001).

including CD8⁺ T cell memory, plasmacytoid DC (pDC) maturation,^{24,25} and human NK cell maturation,²⁶ and the FVB variant may affect a post-translational regulatory domain. Less is known about the functions of *Cyp4f13* and *Umodl*, but *Cyp4f13* is involved in neutrophil chemotaxis and leukotriene B₄ metabolism,^{27–29} and *Umodl* is expressed in proliferating CD4⁺ T cells.³⁰

To eliminate any confounding FVB genetics, we employed a single nucleotide polymorphism (SNP) marker-guided, speed congenic breeding scheme^{31,32} to generate B6 mice with the FVB-Chr17 QTL allele. N2 mice with the FVB-Chr17 QTL allele were further backcrossed to B6 dams for four more generations. At the 5th generation (N5), heterozygous G5 offspring were mated together and G6 pups homozygous

SPLEEN



LIVER

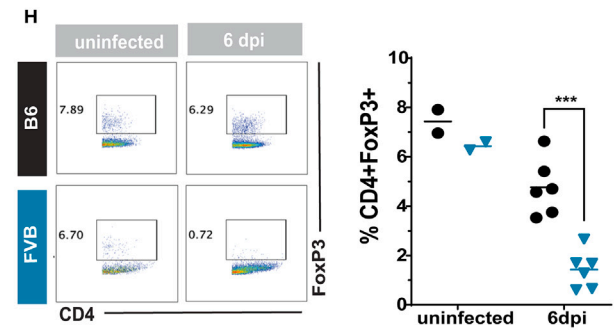
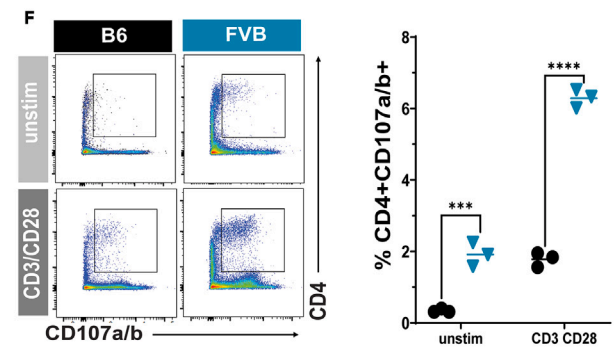
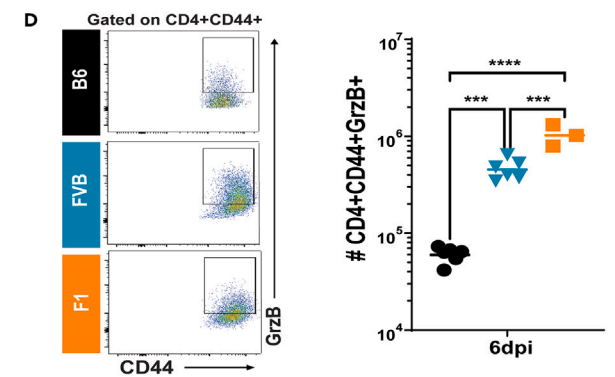
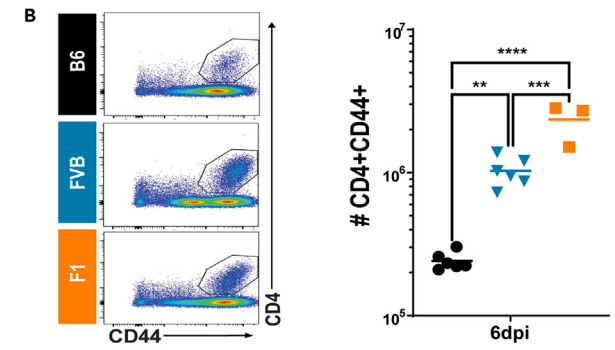


Figure 4. Cl13-infected FVB mice generate a robust granzyme-B+ CD4⁺ T population and lose Treg cells

Leukocytes were isolated from the spleens and livers of Cl13-infected B6, FVB, and F1 mice at 6 dpi and analyzed for their expression of granzyme-B, capacity to degranulate, or their expression of Foxp3.

(A–D) Representative flow plots and total cell count for: (A) CD4⁺CD44^{hi} T cells in spleen, (B) CD4⁺CD44^{hi} T cells in liver, (C) Granzyme-B⁺ (GrzB) cells among CD4⁺CD44⁺ cells in spleen, (D) GrzB⁺ cells among CD4⁺CD44⁺ cells in liver.

(E and F) Single cell suspensions from spleen or liver of B6 or FVB mice were stimulated *ex vivo* with anti-CD3/CD28 or left unstimulated. Samples then stained for surface CD107a and CD107b and analyzed by flow cytometry. (E) Representative flow plots and total frequency of CD107a⁺CD107b⁺ CD4⁺ cells in spleen. (F) Representative flow plots and total frequency of CD107a⁺CD107b⁺ CD4⁺ cells in and liver.

(G) Representative flow plots and total frequency of Foxp3⁺ CD4⁺ T cells in the spleens of uninfected B6 (n = 4) and FVB (n = 5) mice and day 6-infected B6 (n = 6) and FVB (n = 6) mice.

(H) Representative flow plots and total frequency of Foxp3⁺ CD4⁺ T cells in livers of uninfected B6 (n = 2) and FVB (n = 2) mice and infected B6 (n = 6) and FVB (n = 6) mice. All F1 mice were male and B6 and FVB mice were mixed sex. Results are combined from multiple independent experiments with a total of 3–12 mice per strain. All flow cytometry data were gated on live, viability dye-negative cells. Horizontal bars represent mean. Statistical analyses included unpaired one-way ANOVA (A–D) and Student's t test (E–H) (*p < 0.05, **p < 0.01, ***p < 0.001, ****p < 0.0001).

at the Chr17 QTL were selected for interbreeding and maintenance of B6 congenic mice with the FVB allele at the Chr17 QTL. During our breeding, we identified N3 males that showed evidence of meiotic recombination in the interval, as demonstrated by the loss of FVB SNP markers at the proximal end of the original QTL locus (Figure 6D, bottom). These two N3 males were bred independently to B6 over three more generations as above, resulting in three separate G6 lineages. G6 lineages are denoted by the approximate length of their QTL interval: B6.FVB(Chr17:30–55Mb)25/JW (G6_25), B6.FVB(Chr17:31–55Mb)24/JW (G6_24), and B6.FVB(Chr17:35–55Mb)20/JW (G6_20).

G6_24 and G6_25 both exhibited significant lethality (and were not significantly different from each other) compared to B6 mice (Figures 6E and S4C–S4F). The pattern of lethality in G6_24 and G6_25 mice mirrored that of FVB mice. In contrast, G6_20 mice had a greater survival rate (46.3%), approximately equal to N2 and F1 mice. Given the recombination break points in these three congenic lines, it is clear that variants located at ~31–34 Mb are important determinants of outcome. None of the G6 sublines showed significant sex-dependent effects on survival following infection (Figures S4G–S4I), suggesting that the sex-dependent effects observed in the F1 mice (Figure S1A) requires an FVB element(s) outside of the Chr17:30–55Mb region. Regardless of genotype, all G6 mice that succumbed to infection had elevated levels of ALT at the time of euthanasia that were similar in magnitude to levels in FVB mice (Figure 6F), indicating that variants within the ~34–55 Mb region contribute to liver injury.

G6_24 mice, which most closely recapitulated the Cl13-mediated lethality observed for FVB mice, were necropsied on day 6 of infection. These mice displayed marked platelet loss (Figure 6G) and showed histologically similar pathology as previously described for FVB mice (Figures S4J–S4K). The G6_24 mice also generated a robust IFN- γ response at 24 h of infection (Figure 6H), similar to FVB mice,⁸ suggesting the FVB-Chr17 QTL drives elevated IFN- γ responses. In total, our data demonstrate that an FVB allele spanning 30–55 Mb on chromosome 17 promotes lethal pathogenesis during infection, and that some potential causal variants are located at ~31–34Mb.

An FVB allele on chromosome 17 drives early NK-mediated platelet loss and liver damage

We sought to assess whether the same cell types driving pathogenesis in FVB mice were present in G6 mice. Since lethality was most pronounced in G6_24 and G6_25 mice, and was not different between one another, we focused our subsequent analyses on these lines. Both lines were used interchangeably and denoted simply as “G6” hereafter. Data solely from a specific line is noted in figure legends.

Unlike FVB mice, G6 mice did not have increased numbers of NK cells before or at 3 dpi (Figure 7A) compared to B6 mice. NK cells from G6 mice stimulated *ex vivo* with PMA (phorbol 12-myristate 13-acetate) and ionomycin showed levels of degranulation that were comparable to B6 cells, both before and after infection (Figures S5A and S5C). Interestingly, FVB NK cells degranulated less than B6 or G6 NKs despite having a larger Nkp46⁺ NK cell population (Figures S2 and S5). G6 NK cells expressed Nkp46 at levels that were similar to B6 but lower than FVB (Figures S5B and S5D) and expressed GrzB at amounts that were comparable to B6 (Figure S5E). Liver NK cells can be distinguished as tissue resident NK (trNK) cells or conventional NK (cNK) cells (Figure 7B). At 6dpi, G6 mice had significantly more NK1.1⁺CD49a⁺DX5⁻ trNK cells and more Nkp46⁻GrzB⁺ trNK cells than B6 mice (Figures 7C, 7D, and S5F), suggesting that G6 trNKs are more activated during infection. Livers from G6 and B6 mice contained similar numbers of cNK cells (NK1.1⁺CD49a⁻DX5⁺), including GrzB⁺ subsets (Figures 7D and S5F).

NK cells cannot be depleted in FVB mice using anti-NK1.1 (PK136) antibody, because it does not recognize the FVB variant of NK1.1 (data not shown).^{33,34} However, G6 mice are homozygous for the B6 NK1.1 variant of *Klrp1* (on Chr6), and their NK cells can be targeted by PK136. Compared to isotype-treated mice, NK cell-depleted G6 mice showed reduced ALT activity and increased platelet counts at day 3 post infection (Figure 7E), suggesting that the Chr17 locus drives NK cell-mediated liver injury, though it is unclear whether trNK or cNK cell are responsible for these effects.

The FVB allele at chromosome 17 tracks with increased GrzB⁺ T cells and loss of Treg cells

FVB mice showed aberrations in T cells subsets, including increased cytolytic CD4⁺ T cells and decreased Tregs. We assessed whether these T cell alterations occurred in G6 mice. At day 6 post infection, G6 and B6 mice had similar numbers of CD44^{hi} CD4⁺ and CD8⁺ T cells in the spleen, but G6 livers had significantly more of both populations than B6 livers (Figures S6A and S6B). Like FVB mice, G6 mice also displayed an

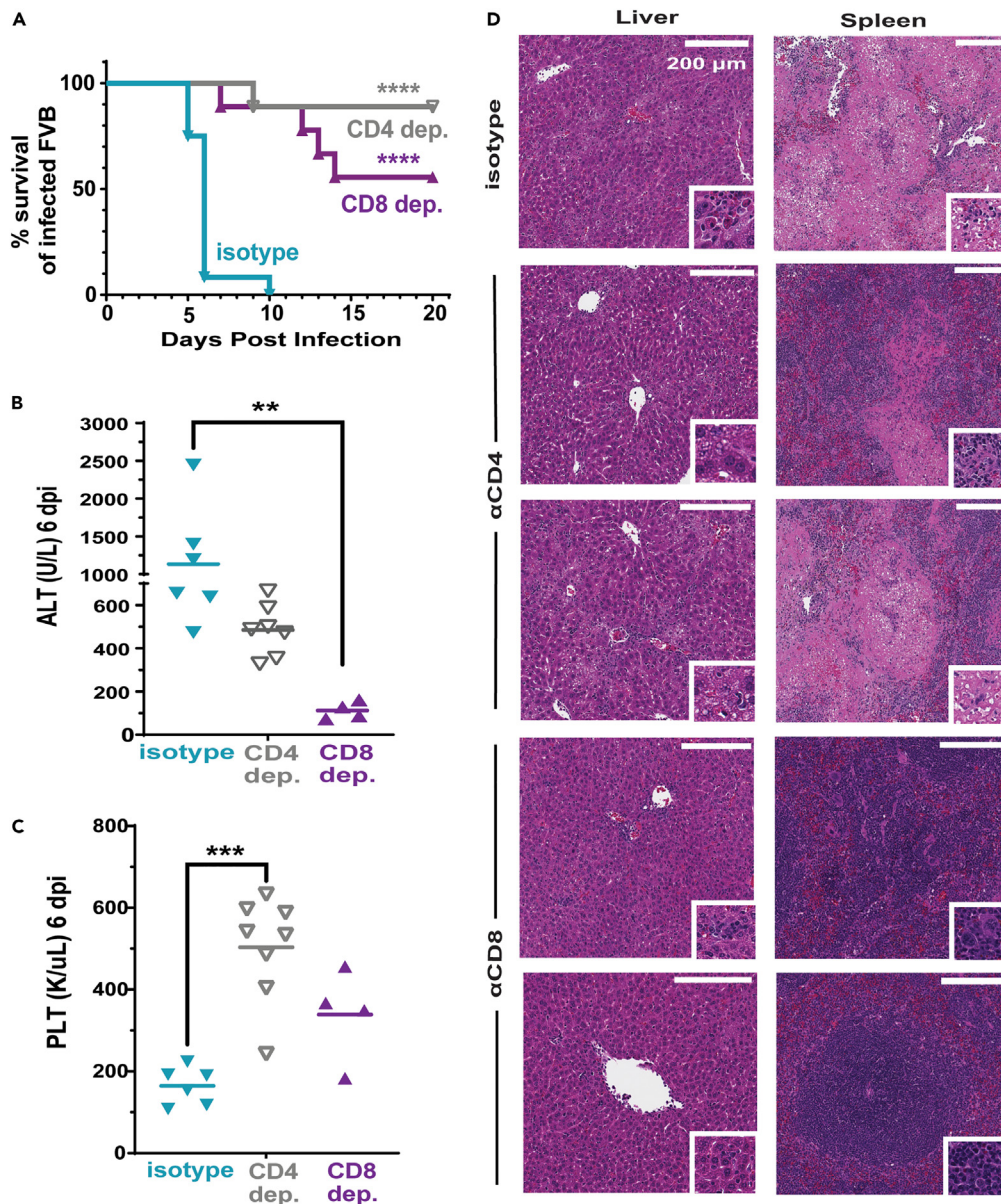


Figure 5. T cells drive pathology and lethality in CI13-infected FVB mice

Cohorts of mixed-sex FVB mice were given depleting antibodies to remove CD4⁺ T cells or CD8⁺ T cells, or were given non-depleting isotype control antibody prior to LCMV-CI13 challenge. The mice were assessed over time for physical signs of illness to criterion endpoints. Other mice were necropsied at day 6 and assessed for blood ALT activity and platelet counts, and spleen and liver histology.

(A) FVB mice were depleted of CD4⁺ T cells (n = 9), CD8⁺ T cells (n = 9), or given isotype-control antibody (n = 10) prior to CI13 challenge and were monitored for survival.

(B) ALT in sera of CD4-depleted (n = 7), CD8-depleted (n = 4), or isotype-treated (n = 6) mice.

(C) Platelet levels of CD4-depleted (n = 8), CD8-depleted (n = 4), or isotype-treated (n = 6) mice.

(D) Representative histology of spleen and liver of mice with isotype or depleting antibody treatment. Each image is from a different mouse. White scale bar represents 200 μ m. White boxed insets provide zoomed-in examples of varying cellular composition. All flow gated on live, viability dye-negative cells. Horizontal bars represent mean. Results from independent experiments were combined. Statistical analyses were Kaplan Meier (A) and unpaired one-way ANOVA (B and C) (*p < 0.05, **p < 0.01, ***p < 0.001, ****p < 0.0001).

increased population of CD4⁺CD44⁺GrzB⁺ T cells in the spleen and liver compared to B6 mice (Figures 8A and 8B) with a greater level of GrzB expression per cell in the liver (Figures S6C and S6D). G6 mice had more liver CD8⁺CD44⁺GrzB⁺ T cells and more CXCR6⁺ cells in the spleen and liver than B6 mice (Figures S6E–S6H).

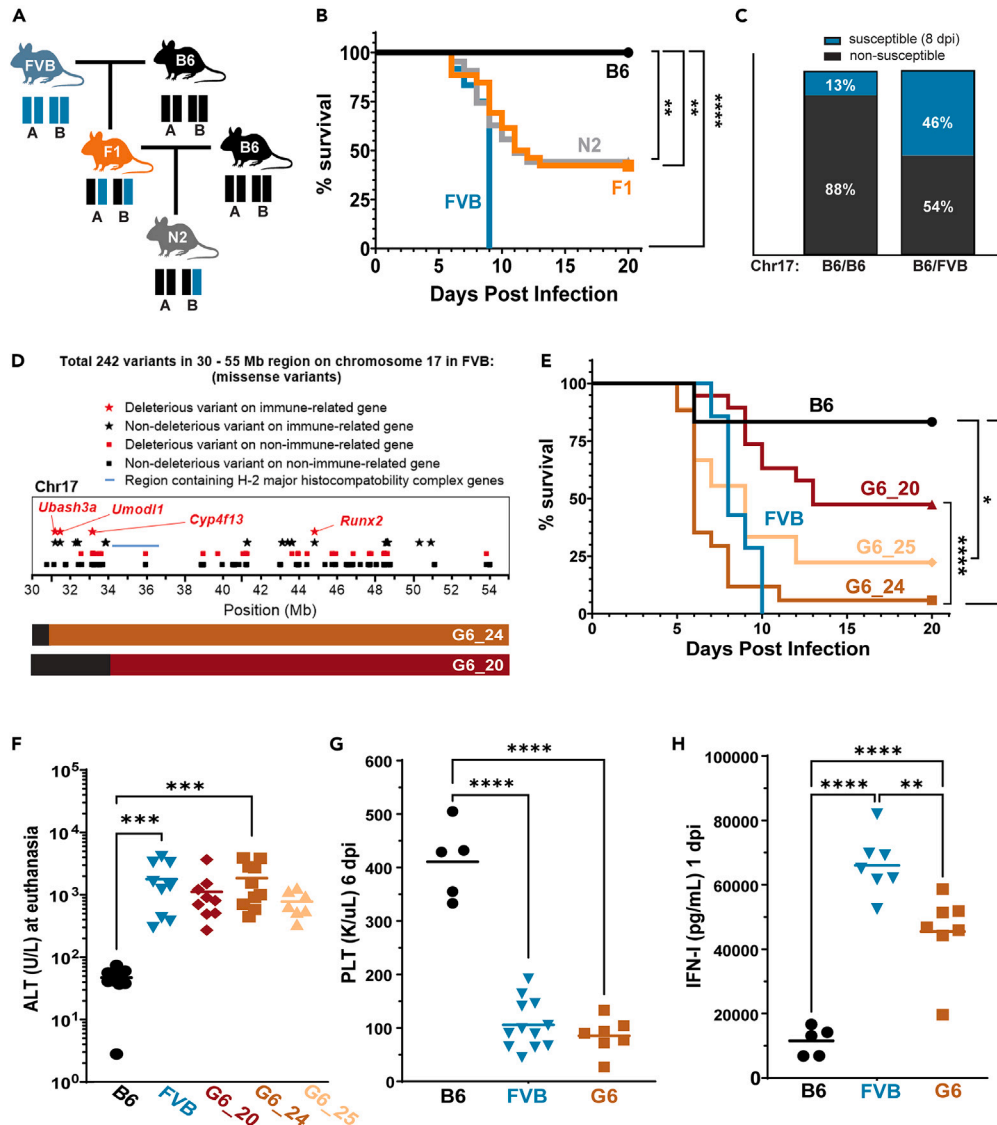


Figure 6. Pathogenesis in FVB mice is linked to a 25Mb locus on chromosome 17

Forward genetics was used to identify the FVB genetics driving pathogenesis after infection. At the N2 generation, mice were challenged and monitored for physical signs of illness. QTL mapping implicated Chr17. Other N2 mice with the FVB allele(s) at Chr17 were selected for further crosses to B6/J mice and then intercrossed to generate G6 mice that were homozygous at Chr17.

(A) Illustration of the breeding scheme showing allele inheritance by generation.

(B) Survival rate of Cl13-infected N2 mice (n = 63) compared to B6 (n = 12), FVB (n = 12), and F1 (n = 26) mice.

(C) The frequency of the FVB allele at chromosome 17 (Chr17) in the 63 N2 mice that did or did not survive post infection.

(D) Missense coding variants along a 25Mb locus at FVB Chr17. Below is an illustration of two lines of FVB-derived G6 mice with different recombination patterns within the original 25Mb Chr17-QTL. Each line is represented as either a light brown (G6_24) or dark reddish-brown bar (G6_20). Black portions of the bars represent sequence analogous to B6.

(E) Survival of G6_20 (n = 19), G6_24 (n = 17), G6_25 (n = 9), FVB (n = 7), and B6 (n = 6) mice post Cl13 infection.

(F) ALT at time of mandatory euthanasia (between 5 and 13 dpi) for G6_20 (n = 9), G6_24 (n = 10), and G6_25 (n = 7) compared to B6 (n = 15) and FVB (n = 9) mice.

(G) Total platelet count of B6 (n = 5), FVB (n = 12), and G6_24 (n = 7) mice at day 6 dpi.

(H) IFN-I levels in sera 24 h post-infection of B6 (n = 5), FVB (n = 7), and G6_24 (n = 7) mice. Horizontal bars represent mean. (F–H) Results were combined from multiple independent experiments and involved mixed sex mice. Statistical analysis used Kaplan Meier (B, E) and one-way ANOVA (F–H) (*p < 0.05, **p < 0.01, ***p < 0.001, ****p < 0.0001).

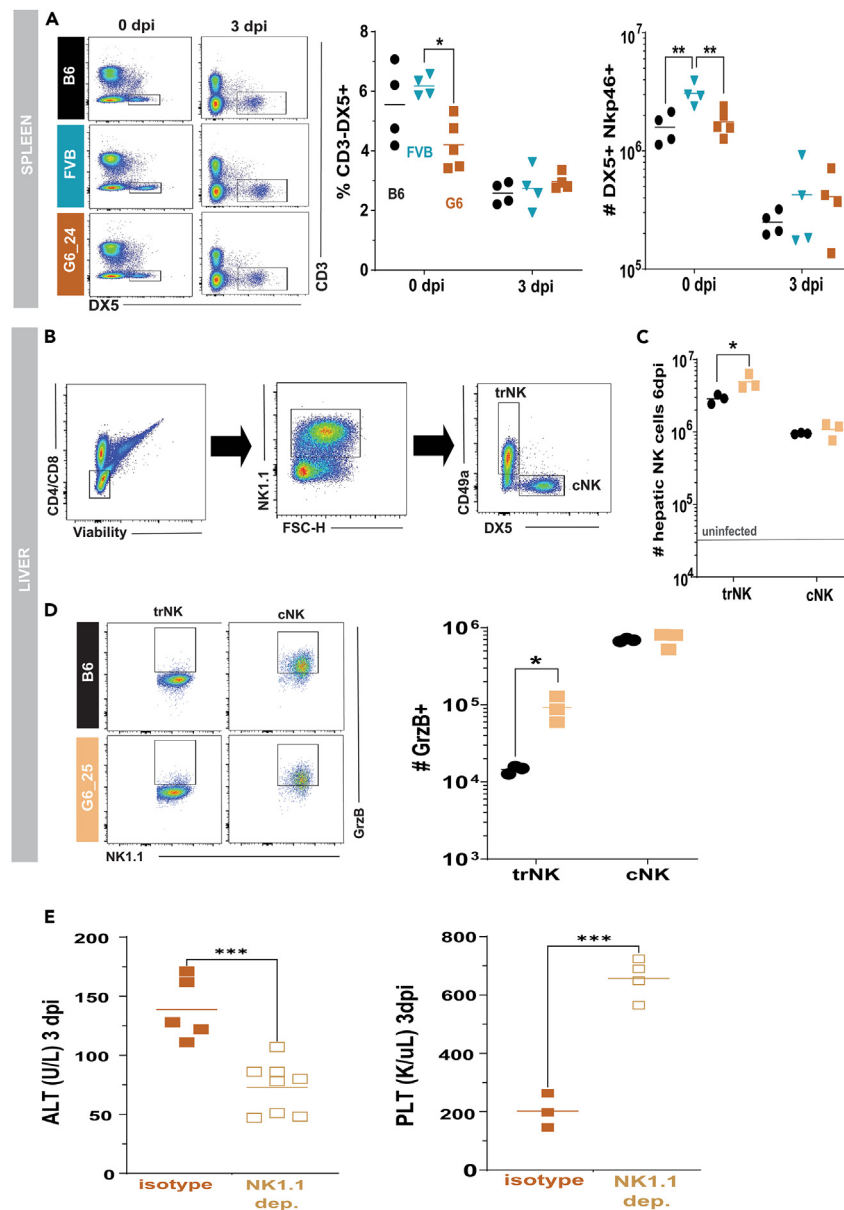


Figure 7. NK cells drive early disease in mice with the FVB-Chr17 QTL

Mixed-sex cohorts of B6, FVB, G6_24 or G6_25 were challenged with LCMV-Cl13 and evaluated via flow cytometry at 0, 3, or 6-day post-infection (dpi) for the frequency of NK cells in spleen and liver. Other cohorts of infected G6 mice were treated with NK cell depleting antibody or isotype-control antibody and were assessed for blood ALT activity and platelet counts at day 3 dpi.

(A) Representative flow plots, total frequency, and total cell count of CD3⁺DX5⁺ NK cells from spleen of B6 (n = 4), FVB (n = 4), and G6 (n = 4–5) mice.

(B–D) Analysis of NK cells from Cl13-infected B6 (n = 3) and G6_25 (n = 3) mice 6 dpi. (B) Gating strategy for discriminating tissue resident NK cells (trNK) and conventional NK cells (cNK). Lymphocyte and doublet discrimination gates not shown. (C) Total cell count of trNK and cNK cells. (D) Representative flow plots of GrzB expression by trNK and cNK cells.

(E) G6_24 mice were given either isotype (n = 5) or NK1.1-depleting antibody (n = 8) prior to infection and ALT was recorded in the sera 3 dpi (left). G6_24 mice were given either isotype (n = 3) or NK1.1-depleting antibody (n = 4) prior to infection and total blood platelet count was recorded 3 dpi (right). All flow gated on live, viability dye-negative, singlet cells. Horizontal bars represent mean. Statistical analyses used unpaired one-way ANOVA (A) and unpaired student's t-tests (C–E) (*p < 0.05, **p < 0.01, ***p < 0.001, ****p < 0.0001).

G6 mice were significantly protected from death when CD8⁺ T cells were depleted, and CD4⁺ T cell depletion showed a similar trend (Figure 8C). CD8⁺ T cell depletion reduced ALT activity and improved platelet counts, whereas CD4⁺ T cell depletion failed to rescue platelet loss or reduce ALT levels in infected G6 mice (Figures 8D and 8E), suggesting that the FVB-Chr17 allele drives a more dominant

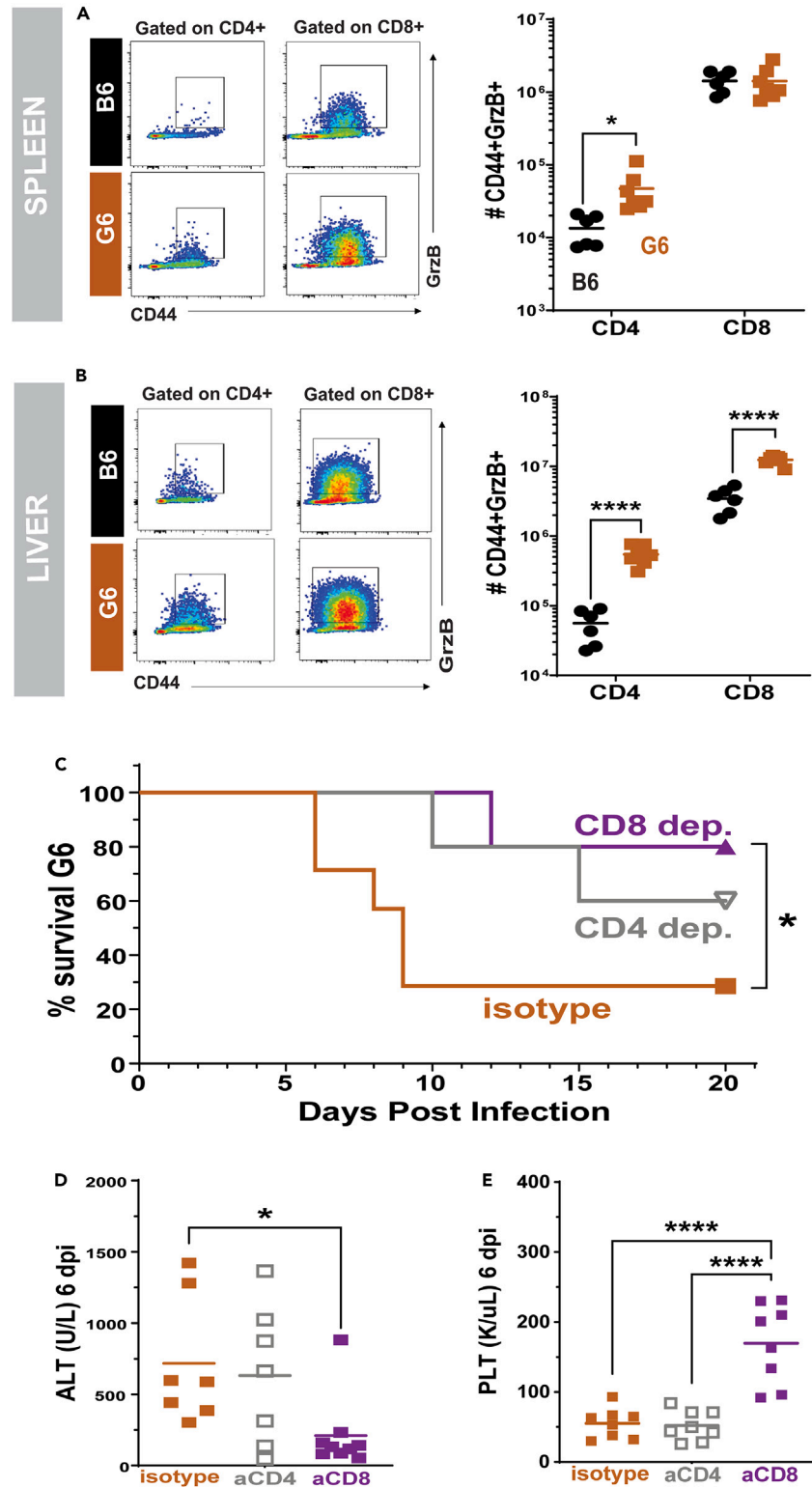


Figure 8. The FVB-Chr17 QTL drives increased cytotoxic T cell populations, pathogenesis, and lethality

Cohorts of B6, G6_24, or G6_25 mice were challenged with LCMV-Cl13 and the frequency and total number of granzyme-B⁺ T cells in spleen and liver was assessed at day 6 post-infection.

(A) Representative flow plots, total frequency, and total cell count of CD4⁺CD44⁺GrzB⁺ cells in spleen.

Figure 8. Continued

(B) Representative flow plots, total frequency, and total cell count of CD4⁺CD44⁺GrzB⁺ cells in liver.

(C–E) Groups of G6_24 mice were treated with isotype (n = 7), anti-CD4- (n = 5), or anti-CD8-depleting (n = 5) antibodies and then challenged with LCMV-Cl13. (C) Survival of G6_24 mice across time post-infection. (B) ALT at day 6 post-infection in G6 mice treated with isotype, CD4-, or CD8-depletion antibody. (C) Platelet counts at day 6 in blood of G6 mice treated with isotype, CD4-, or CD8-depletion antibody. All flow gated on viability dye-negative, singlet cells. Horizontal bars represent mean. Statistical analyses used Kaplan Meier (C), unpaired Student's t test (A and B), or one-way ANOVA (D and E) (*p < 0.05, **p < 0.01, ***p < 0.001, ****p < 0.0001).

CD8⁺ T cell phenotype. Previously, we and others showed in B6 mice that NK cell depletion improves virus-specific T cell responses from day 8 onwards during Cl13 infection.^{35–39} Because G6 mice show NK cell-dependent and T cell-dependent pathogenesis, we considered whether NK cell depletion would improve outcomes. The NK1.1-depleting antibody eliminated mature NK1.1⁺DX5⁺ cells from both spleen and liver, though a residual population of NK1.1⁺DX5⁻ remained at 6dpi (Figures S7A and S7B). These NK1.1⁺DX5⁻ cells lacked the activation markers Nkp46 and GrzB (data not shown), suggesting they are repopulating immature or trNK cells and do not exhibit cytolytic effector functions.

NK-depleted mice showed a trend toward increased number of GrzB⁺ T cells by 6 days of infection (Figures S7C and S7G). Higher frequency of IFNγ⁺ CD8⁺ T cells in the spleen and liver of G6 mice (Figures S7D and S7H), and more CXCR3⁺ T cells, with the most significant increase in the liver (Figures S7E, S7F, S7I, and S7J). In sum, removing NK cells reduces early ALT and rescues platelet frequencies (Figure 7E); however, by further expanding T cell responses, NK-depletion would likely worsen T cell-mediated pathogenesis (Figures 5A–5C and 8C–8E), as is known to occur in B6 mice.

G6 mice had normal frequencies of Treg cells prior to infection, but drastically lost these cells after infection (Figures 9A and 9D), resembling FVB mice. Considering total number of Tregs and effector T cells, the ratio of Tregs to activated CD4⁺ T cells alone (not including CD8⁺ T cells) was greatly reduced in the spleen and liver of G6 mice compared to B6 (Figures 9B, 9C, 9E, and 9F). Interestingly, compared to B6 CD4⁺ T cells, both G6 and FVB CD4⁺ T cells had a reduced capacity to form Tregs under *in vitro* conditions (Figure 9G), suggesting the FVB-Chr17 QTL functions within T cells to impact Treg differentiation.

In summary, these data show that the FVB allele at Chr17:30-55Mb drives spleen and liver pathogenesis during infection that ultimately leads to death. This is associated with pathogenic NK cell responses, a robust loss of Tregs, and an outgrowth of activated cytolytic T cells. Genetic variants at this locus represent new candidate regulators of cytotoxic and pro-inflammatory cell populations that mediate hemorrhagic disease pathogenesis.

DISCUSSION

A subset of people who are exposed to arenavirus infections will develop hemorrhagic disease, which typically involves multi-organ injury. These infections often result in respiratory distress and substantial liver injury. There are few animal models that fully recapitulate human hemorrhagic disease symptoms; however, Cl13-infected FVB and G6 mice develop key features of human disease and can be useful for studies of virus-induced hemorrhagic disease pathology. The G6 mice, which are congenic to B6, are useful for mechanistic cellular and molecular studies of viral pathogenesis or for testing novel approaches to limit tissue injury. We find that an FVB allele at Chr17:30-55Mb is responsible for liver pathogenesis upon Cl13 infection, which is characterized by loss of platelets, liver injury that is biphasic over the course of infection, and lethality. Hepatitis during infection is associated with elevated pDC frequencies and type-1 interferon production, pathogenic NK cell responses in the liver, as well as T cell responses that deviate from those found in B6 mice. The G6 mice generated in this study can be used for future studies to characterize the genetic and molecular basis for the altered immune phenotypes that emerge during infection.

FVB and G6 mice produce copious amounts of IFN-I in response to Cl13 infection and lethality is IFNAR1-dependent in FVB mice.⁹ FVB and G6_24 mice have more pDCs (Figure S2A and data not shown), which are the main cells responsible for early IFN-I production during LCMV infection.^{14,40} This strong type-1 interferon response may promote NK cell reactivity and NK cell-dependent early liver injury. Despite the similar NK responses and profiles to B6 mice, NK depletion improved platelet counts and reduced early liver injury in infected G6 mice. It is possible that pDC-derived IFN-I exaggerates early NK cell-dependent liver pathogenesis. However, NK-depleted G6 mice tended to have more activated T cells, compared to NK-replete G6 mice, a finding that echoes previous results in B6 mice. Thus, our findings related to NK cells in FVB and G6 mice differ dramatically from what we and others have described for NK cells in B6 mice, where NK cells did not cause liver injury but only exerted an immunoregulatory function that protected mice from pathogenesis by dampening T cell responses to LCMV.^{35–39,41} These findings with the same dose and strain of virus illustrates how NK cell biology can vary greatly based on the genotype of mice.

Late-stage liver injury in FVB and G6 mice was driven by both CD4⁺ and CD8⁺ T cells. In B6 mice, CD4⁺ T cells largely play a supportive role, expressing costimulatory molecules and cytokines to augment the antiviral CD8⁺ T cell response or provide help to B cell responses. However, in FVB and G6 mice, there was a significantly elevated population of GrzB-expressing CD4⁺ T cells in the liver that were capable of degranulating. It may be that this large population of CD4⁺GrzB⁺ T cells directly contributes to pathology in FVB and G6 mice, though we do not know the underlying mechanism by which these cells cause liver injury. We have observed MHCII (H-2q) expression on hepatocytes isolated from uninfected and Cl13-infected FVB mice (data not shown), suggesting that direct cognate interactions between CD4⁺ T cells and hepatocytes may occur. Kupffer cells are MHCII⁺, but it is unclear how CD4⁺ T cell-mediated destruction of these cells alone would result in catastrophic liver injury.

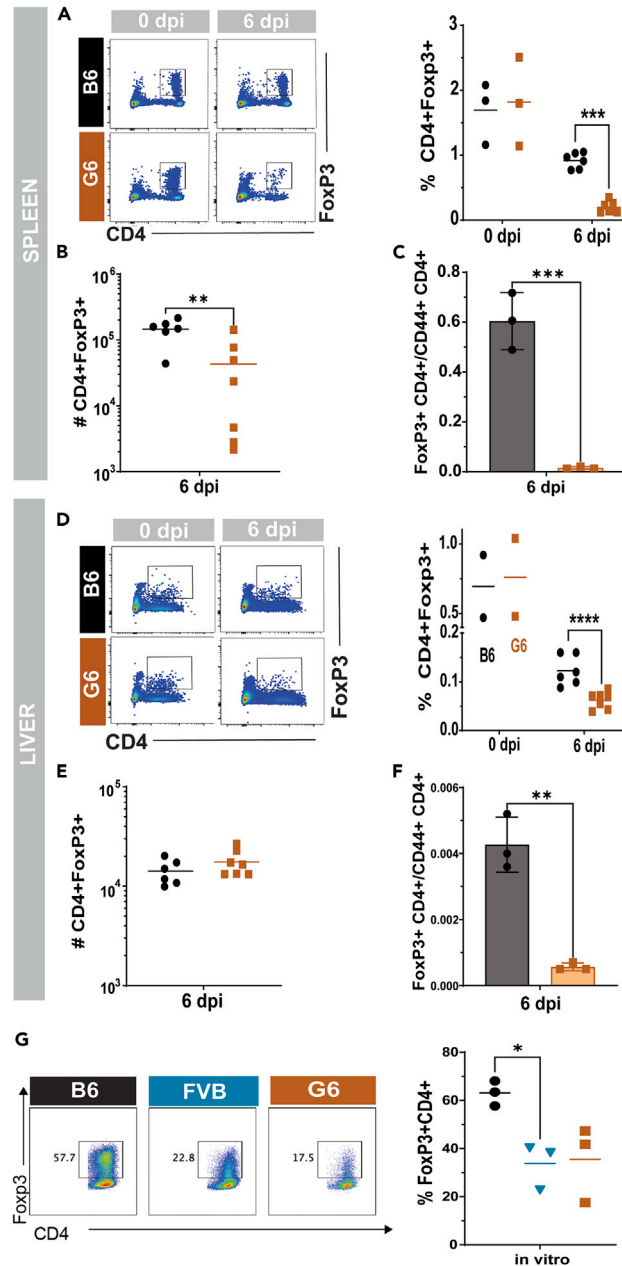


Figure 9. The FVB-Chr17 QTL drives loss and dysfunction of Tregs

CD4⁺Foxp3⁺ Treg cells were quantified in the spleens and livers of mixed sex B6 and G6 mice before and 6-day post-infection (dpi).

(A) Representative flow plots identify CD4⁺Foxp3⁺ cells in spleen; the graph shows their frequency among all CD4⁺ cells.

(B) The number of CD4⁺Foxp3⁺ cells per spleen at 6 dpi.

(C) Ratio of the number of splenic CD4⁺Foxp3⁺ cells to the total number of activated CD4⁺CD44⁺ cells.

(D) Representative flow plots and frequency of CD4⁺Foxp3⁺ cells in liver.

(E) Total number of CD4⁺Foxp3⁺ cells 6 dpi.

(F) Ratio of CD4⁺Foxp3⁺ cells to all activated CD4⁺CD44⁺ cells in the liver.

(G) CD4⁺ T cells from B6 (n = 3), FVB (n = 3), or G6₂₄ (n = 3) mice were purified and cultured under T regulatory (Treg) conditions with IL-2 and TGFβ for three days. Data combined from three independent experiments (n = 1 mouse/experiment). Representative flow plots depict Foxp3 expression by CD4⁺ T cells of each genotype (left). The frequency of Foxp3⁺ cells among live CD4⁺ cells (right). The FACS analyses were gated on viability dye-negative, singlet cells. Horizontal bars represent mean (A, B, D, E, and G). Data are represented as mean ± SEM (C, F). Results from multiple experiments are combined. Significance was determined by unpaired Student's t test (A–F) or one-way ANOVA (G) (*p < 0.05, **p < 0.01, ***p < 0.001, ****p < 0.0001).

Despite T cells driving late-stage pathology in both FVB and G6 mice, FVB mice had fewer CD8⁺ T cells compared to B6 mice whereas G6 mice had more CD8⁺ T cells than B6 mice. Thus the number of CD8⁺ T cells alone did not correspond to lethality. One explanation is that increased expression of Nkp46 on FVB NK cells (but not G6) may contribute to the loss of effector CD8⁺ T cells.^{39,41} Another possibility is the robust destruction of lymphoid architecture in the tissues of FVB mice leads to the collapse of a structurally organized T cell response.

Interestingly, FVB and G6 mice experienced a profound loss of Tregs in the spleen and liver after infection, perhaps allowing for enhanced immune cell recruitment and tissue injury. The loss of the Treg cells might be linked to the elevated IFN-I made early on during infection.⁴² However, the FVB-Chr17 QTL impaired the *in vitro* transition of CD4⁺ T cells to Foxp3⁺ cells (Figure 9G), suggesting that the Treg cells in these mice are intrinsically dysfunctional.

We noted sex dependent differences in pathogenesis of F1 mice, where all males, but only 25% of females required euthanasia. This sex difference occurred regardless of parent of origin (Figure S1). As F1-derivative mice were further backcrossed to B6 mice, the influence of sex on infection outcome diminished and was lost by the sixth generation (G6) (Figure S4). These data imply that additional loci outside of the FVB-Chr17 QTL influence susceptibility to disseminated infection.

The susceptibility of mice to CI13 was linked to an FVB allele at Chr17(30-55Mb). Lethality and pathogenesis were reproduced independently in three separate lines of G6 mice, most significantly in G6_24 and G6_25. G6_20 mice showed improved survival compared to G6_24 and G6_25 lines, indicating a proximal QTL region (~31-34Mb) containing variants that significantly impact lethality following CI13 infection. Additional variants located more distal in the QTL region likely explain the remaining susceptibility. The FVB-Chr17 QTL in total includes the MHC, however, we do not think H-2^q alone is linked to pathogenesis, because SWR/J mice, which also have the H-2^q haplotype, fail to develop hemorrhagic disease when infected with CI13.⁸ Nevertheless, the MHC haplotype can affect the susceptibility of mice to LCMV infection on varying genetic backgrounds⁴³⁻⁴⁵ and therefore cannot be ruled out as a contributing factor. While we have not excluded the possibility of non-coding genetic elements affecting susceptibility, we have identified multiple missense coding variants within this QTL with relevant biological annotations predicted to impact gene function. Notably, genetic variation near these genes has also been associated with differences in white blood cell counts in humans, including associations for variants near *UBASH3A*, *UMODL1*, *RUNX2*, and *CYP3A5*.⁴⁶ As an aside, our findings for FVB and G6 mice differ somewhat from our previous findings with PL/J mice, which acquire severe lung edema due to genetic variants at Chr9, yet show minimal liver injury.¹³ Thus, even among lines of mice that are susceptible to the same virus, host genetics determines tissue-specific mechanisms of pathogenesis.

Previous studies have shown that FVB mice succumb to CI13 infection.^{7,8} We confirm that the infection is lethal, associated with loss of platelets, that CD8⁺ T cell depletion protects against pathogenesis, and that FVB mice produce elevated amounts of IFN-I. However, we noted several differences with these earlier studies and extended those analyses in substantial ways. The earlier reports did not report sex differences in infection outcome, whereas we show the FVB genetic background affects susceptibility in a sex-dependent manner, with F1 and N2 males perishing more than females. Importantly, we did not observe substantial lung injury (day 6) unless the mice were moribund (>day 7). Instead, we found that livers were greatly impacted by infection and that liver injury was biphasic, with NK cells contributing to pathogenesis early on and GrzB⁺CD4⁺ T cells contributing later. Mouse survival improved when CD4⁺ T cells were depleted, a finding shared by one group⁷ but not the other.⁸ Beyond previous studies, we observed that FVB and G6 CD4⁺ T cells were altered in differentiation. In addition to accumulating GrzB⁺CD4⁺ T cells, FVB and G6 CD4⁺ T cells failed to differentiate into Treg cells *in vitro* or to persist as Treg cells *in vivo* during infection. These results suggest that the FVB-Chr17 QTL may have a cell-intrinsic impact on T cell differentiation. Finally, we linked infection pathogenesis to an FVB allele at Chr17.

Overall, we have identified a region on FVB-Chr17 that controls cell intrinsic, innate, and adaptive immune responses to disseminated infection. A limited number of genetic variants at this locus result in inflammatory responses, including the induction of pathogenic NK cells, the loss of Treg cells, outgrowth of granzyme-B⁺ CD4⁺ T cells, and liver pathogenesis. We anticipate that further characterization of these genetic variants will improve our understanding of how NK cells, Treg cells, and cytolytic CD4⁺ T cells develop and how liver injury unfolds during virus infection.

Limitations of the study

The QTL identified here has only been analyzed for variants in protein-encoding elements. Other non-protein-encoding elements may also contribute to disease and lethality. Differences in MHC haplotype between B6, FVB, and G6 mice may influence the variation and intensity of immune responses among the three genotypes.

STAR★METHODS

Detailed methods are provided in the online version of this paper and include the following:

- KEY RESOURCES TABLE
- RESOURCE AVAILABILITY
 - Lead contact
 - Materials availability
 - Data and code availability
- EXPERIMENTAL MODEL AND SUBJECT DETAILS

- Mice
- Breeding
- Virus
- Cell culture
- **METHOD DETAILS**
 - Genotyping and quantitative trait locus (QTL) mapping
 - PCR genotyping
 - Variant analysis
 - Complete blood count (CBC) and alanine transferase (ALT)
 - Histology
 - *In vivo* depletions of cells
 - Cell isolation and purification
 - Flow cytometry
 - T cell degranulation
 - NK cell degranulation
 - *In vitro* CD4 differentiation
 - CD4 subset stimulation and staining
- **QUANTIFICATION AND STATISTICAL ANALYSIS**

SUPPLEMENTAL INFORMATION

Supplemental information can be found online at <https://doi.org/10.1016/j.isci.2023.108348>.

ACKNOWLEDGMENTS

Dr. Stephanie Montgomery (UNC, Animal Histopathology & Laboratory Medicine Core) provided helpful guidance and expertise on histological analyses. Ling Wang (UNC, Animal Histopathology & Laboratory Medicine Core) performed complete blood count (CBC) and alanine transferase (ALT) measurements. The Animal Histopathology & Laboratory Medicine core and the UNC Flow Cytometry Core were supported by an NCI Center Core Support Grant (5P30CA016086–41) to the Lineberger Comprehensive Cancer Center. L.J.D. was supported by NIH F31HL143853. This research was supported by NIH awards R01AI138337, R01AI143894, R01AI131685, and a DoD award W81XWH2110919 to J.K.W.

AUTHOR CONTRIBUTIONS

T.N.T., A.A.B., and J.K.W. designed experiments and analyzed the resulting data. T.N.T., A.A.B., M.D., and I.M. performed experiments, mouse breeding, genotyping, plaque assays, and T cell analyses. QTL analyses were performed by L.J.D., T.N.T., M.T.F., and S.N.P.K. T.N.T. and J.K.W. wrote the manuscript with input from all authors. The research was supervised by J.K.W.

DECLARATION OF INTERESTS

The authors declare no competing interests.

Received: March 9, 2023

Revised: September 19, 2023

Accepted: October 23, 2023

Published: October 28, 2023

REFERENCES

1. Sarute, N., and Ross, S.R. (2017). New World Arenavirus Biology. *Annu. Rev. Virol.* 4, 141–158. <https://doi.org/10.1146/annurev-virology-101416-042001>.
2. Ogbu, O., Ajuluchukwu, E., and Uneke, C.J. (2007). Lassa fever in West African sub-region: An overview. *J. Vector Borne Dis.* 44, 1–11.
3. Mateer, E.J., Huang, C., Shehu, N.Y., and Paessler, S. (2018). Lassa fever-induced sensorineural hearing loss: A neglected public health and social burden. *PLoS Neglected Trop. Dis.* 12, e0006187. <https://doi.org/10.1371/journal.pntd.0006187>.
4. Smith, D.R., Holbrook, M.R., and Gowen, B.B. (2014). Animal models of viral hemorrhagic fever. *Antivir. Res.* 112, 59–79. <https://doi.org/10.1016/j.antiviral.2014.10.001>.
5. Gowen, B.B., and Holbrook, M.R. (2008). Animal models of highly pathogenic RNA viral infections: Hemorrhagic fever viruses. *Antivir. Res.* 78, 79–90. <https://doi.org/10.1016/j.antiviral.2007.10.002>.
6. Utzschneider, D.T., Alfei, F., Roelli, P., Barras, D., Chennupati, V., Darbre, S., Delorenzi, M., Pinschewer, D.D., and Zehn, D. (2016). High antigen levels induce an exhausted phenotype in a chronic infection without impairing T cell expansion and survival. *J. Exp. Med.* 213, 1819–1834. <https://doi.org/10.1084/jem.20150598>.
7. Schnell, F.J., Sundholm, S., Crumley, S., Iversen, P.L., and Mourich, D.V. (2012). Lymphocytic Choriomeningitis Virus Infection in FVB Mouse Produces Hemorrhagic Disease. *PLoS Pathog.* 8, e1003073. <https://doi.org/10.1371/journal.ppat.1003073>.
8. Oldstone, M.B.A., Ware, B.C., Horton, L.E., Welch, M.J., Aiolfi, R., Zarpellon, A., Ruggeri, Z.M., and Sullivan, B.M. (2018). Lymphocytic choriomeningitis virus Clone 13 infection causes either persistence or acute death dependent on IFN-1, cytotoxic T lymphocytes (CTLs), and host genetics. *Proc. Natl. Acad. Sci. USA* 115, E7814–E7823. <https://doi.org/10.1073/pnas.1804674115>.

9. Odermatt, B., Eppler, M., Leist, T.P., Hengartner, H., and Zinkernagel, R.M. (1991). Virus-triggered acquired immunodeficiency by cytotoxic T-cell-dependent destruction of antigen-presenting cells and lymph follicle structure. *Proc. Natl. Acad. Sci. USA* **88**, 8252–8256. <https://doi.org/10.1073/pnas.88.18.8252>.
10. Sevilla, N., Kunz, S., Holz, A., Lewicki, H., Homann, D., Yamada, H., Campbell, K.P., De La Torre, J.C., and Oldstone, M.B. (2000). Immunosuppression and resultant viral persistence by specific viral targeting of dendritic cells. *J. Exp. Med.* **192**, 1249–1260. <https://doi.org/10.1084/jem.192.9.1249>.
11. Smelt, S.C., Borrow, P., Kunz, S., Cao, W., Tishon, A., Lewicki, H., Campbell, K.P., and Oldstone, M.B. (2001). Differences in Affinity of Binding of Lymphocytic Choriomeningitis Virus Strains to the Cellular Receptor α -Dystroglycan Correlate with Viral Tropism and Disease Kinetics. *J. Virol.* **75**, 448–457. <https://doi.org/10.1128/jvi.75.1.448-457.2001>.
12. Puglielli, M.T., Browning, J.L., Brewer, A.W., Schreiber, R.D., Shieh, W.J., Altman, J.D., Oldstone, M.B., Zaki, S.R., and Ahmed, R. (1999). Reversal of virus-induced systemic shock and respiratory failure by blockade of the lymphotoxin pathway. *Nat. Med.* **5**, 1370–1374. <https://doi.org/10.1038/70938>.
13. Misumi, I., Cook, K.D., Mitchell, J.E., Lund, M.M., Vick, S.C., Lee, R.H., Uchimura, T., Bergmeier, W., Mieczkowski, P., Pardo-Manuel de Villena, F., et al. (2019). Identification of a Locus in Mice that Regulates the Collateral Damage and Lethality of Virus Infection. *Cell Rep.* **27**, 1387–1396.e5. <https://doi.org/10.1016/j.celrep.2019.04.004>.
14. Cervantes-Barragan, L., Lewis, K.L., Firner, S., Thiel, V., Hugues, S., Reith, W., Ludwig, B., and Reis, B. (2012). Plasmacytoid dendritic cells control T-cell response to chronic viral infection. *Proc. Natl. Acad. Sci. USA* **109**, 3012–3017. <https://doi.org/10.1073/pnas.1117359109>.
15. Nguyen, K.B., Salazar-Mather, T.P., Dalod, M.Y., Van Deusen, J.B., Wei, X.q., Liew, F.Y., Caligiuri, M.A., Durbin, J.E., and Biron, C.A. (2002). Coordinated and Distinct Roles for IFN- α , IL-12, and IL-15 Regulation of NK Cell Responses to Viral Infection. *J. Immunol.* **169**, 4279–4287. <https://doi.org/10.4049/jimmunol.169.8.4279>.
16. Madera, S., Rapp, M., Firth, M.A., Beilke, J.N., Lanier, L.L., and Sun, J.C. (2016). Type I IFN promotes NK cell expansion during viral infection by protecting NK cells against fratricide. *J. Exp. Med.* **213**, 225–233. <https://doi.org/10.1084/jem.20150712>.
17. Havenar-Daughton, C., Kolumam, G.A., and Murali-Krishna, K. (2006). Cutting Edge: The Direct Action of Type I IFN on CD4 T Cells Is Critical for Sustaining Clonal Expansion in Response to a Viral but Not a Bacterial Infection. *J. Immunol.* **176**, 3315–3319. <https://doi.org/10.4049/jimmunol.176.6.3315>.
18. Kolumam, G.A., Thomas, S., Thompson, L.J., Sprent, J., and Murali-Krishna, K. (2005). Type I interferons act directly on CD8 T cells to allow clonal expansion and memory formation in response to viral infection. *J. Exp. Med.* **202**, 637–650. <https://doi.org/10.1084/jem.20050821>.
19. McLaren, W., Gil, L., Hunt, S.E., Riat, H.S., Ritchie, G.R.S., Thormann, A., Flicek, P., and Cunningham, F. (2016). The Ensembl Variant Effect Predictor. *Genome Biol.* **17**, 122–214. <https://doi.org/10.1186/s13059-016-0974-4>.
20. Ng, P.C., and Henikoff, S. (2003). SIFT: Predicting amino acid changes that affect protein function. *Nucleic Acids Res.* **31**, 3812–3814. <https://doi.org/10.1093/nar/gkg509>.
21. Li, Y., Cheng, H., Xiao, F.L., Liang, B., Zhou, F.S., Li, P., Zheng, X.D., Sun, L.D., Yang, S., and Zhang, X.J. (2017). Association of UBASH3A gene polymorphism and atopic dermatitis in the Chinese Han population. *Gene Immun.* **18**, 158–162. <https://doi.org/10.1038/gene.2017.15>.
22. Ge, Y., Paisie, T.K., Newman, J.R.B., McIntyre, L.M., and Concannon, P. (2017). UBASH3A mediates risk for type 1 diabetes through inhibition of T-cell receptor-induced NF- κ B signaling. *Diabetes* **66**, 2033–2043. <https://doi.org/10.2337/db16-1023>.
23. San Luis, B., Sondgeroth, B., Nassar, N., and Carpino, N. (2011). Sts-2 is a phosphatase that negatively regulates Zeta-associated Protein (ZAP)-70 and T cell receptor signaling pathways. *J. Biol. Chem.* **286**, 15943–15954. <https://doi.org/10.1074/jbc.M110.177634>.
24. Olesin, E., Nayar, R., Saikumar-Lakshmi, P., and Berg, L.J. (2018). The Transcription Factor Runx2 Is Required for Long-Term Persistence of Antiviral CD8 + Memory T Cells. *ImmunoHorizons* **2**, 251–261. <https://doi.org/10.4049/immunohorizons.1800046>.
25. Sawai, C.M., Sisirak, V., Ghosh, H.S., Hou, E.Z., Ceribelli, M., Staudt, L.M., and Reis, B. (2013). Transcription factor Runx2 controls the development and migration of plasmacytoid dendritic cells. *J. Exp. Med.* **210**, 2151–2159. <https://doi.org/10.1084/jem.20130443>.
26. Wahlen, S., Matthijssens, F., Loocke, W.V., Taveirne, S., Kiekens, L., Persyn, E., Van Ammel, E., De Vos, Z., De Munter, S., Matthys, P., et al. (2022). The transcription factor RUNX2 drives the generation of human NK cells and promotes tissue residency. *Elife* **11**, 25.
27. Le Bel, M., Brunet, A., and Gosselin, J. (2014). Leukotriene B4, an endogenous stimulator of the innate immune response against pathogens. *J. Innate Immun.* **6**, 159–168. <https://doi.org/10.1159/000353694>.
28. Vaivoda, R., Vaine, C., Boerstler, C., Galloway, K., and Christmas, P. (2015). CYP4F18-Deficient Neutrophils Exhibit Increased Chemotaxis to Complement Component C5a. *J. Immunol. Res.* **2015**, 250456. <https://doi.org/10.1155/2015/250456>.
29. Ye, Z.N., Wu, L.Y., Liu, J.P., Chen, Q., Zhang, X.S., Lu, Y., Zhou, M.L., Li, W., Zhang, Z.H., Xia, D.Y., et al. (2018). Inhibition of leukotriene B4 synthesis protects against early brain injury possibly via reducing the neutrophil-generated inflammatory response and oxidative stress after subarachnoid hemorrhage in rats. *Behav. Brain Res.* **339**, 19–27. <https://doi.org/10.1016/j.bbr.2017.11.011>.
30. Wang, W., Tang, Y., Ni, L., Kim, E., Jongwutiwes, T., Hourvitz, A., Zhang, R., Xiong, H., Liu, H.C., and Rosenwaks, Z. (2012). Overexpression of Uromodulin-like 1 accelerates follicle depletion and subsequent ovarian degeneration. *Cell Death Dis.* **3**, 4333–e514. <https://doi.org/10.1038/cddis.2012.169>.
31. Markel, P., Shu, P., Ebeling, C., Carlson, G.A., Nagle, D.L., Smutko, J.S., and Moore, K.J. (1997). Theoretical and empirical issues for marker-assisted breeding of congenic mouse strains. *Nat. Genet.* **17**, 280–284.
32. Wakeland, E., Morel, L., Achey, K., Yui, M., and Longmate, J. (1997). Speed congenics: A classic technique in the fast lane (relatively speaking). *Immunol. Today* **18**, 472–477. [https://doi.org/10.1016/S0167-5699\(97\)01126-2](https://doi.org/10.1016/S0167-5699(97)01126-2).
33. Carlyle, J.R., Mesci, A., Ljutic, B., Belanger, S., Tai, L.-H., Rousselle, E., Troke, A.D., Proteau, M.-F., and Makrigiannis, A.P. (2006). Molecular and Genetic Basis for Strain-Dependent NK1.1 Alloreactivity of Mouse NK Cells. *J. Immunol.* **176**, 7511–7524. <https://doi.org/10.4049/jimmunol.176.12.7511>.
34. Aguilar, O.A., Berry, R., Rahim, M.M.A., Reichel, J.J., Popović, B., Tanaka, M., Fu, Z., Balaji, G.R., Lau, T.N.H., Tu, M.M., et al. (2017). A Viral Immuno-evasin Controls Innate Immunity by Targeting the Prototypal Natural Killer Cell Receptor Family. *Cell* **169**, 58–71.e14. <https://doi.org/10.1016/j.cell.2017.03.002>.
35. Cook, K.D., Waggoner, S.N., and Whitmire, J.K. (2014). NK cells inhibit humoral immunity by reducing the abundance of CD4 + T follicular helper cells during a chronic virus infection. *Crit. Rev. Immunol.* **34**, 359–388. <https://doi.org/10.1615/CritRevImmunol.2014010604>.
36. Cook, K.D., and Whitmire, J.K. (2013). The Depletion of NK Cells Prevents T Cell Exhaustion to Efficiently Control Disseminating Virus Infection. *J. Immunol.* **190**, 641–649. <https://doi.org/10.4049/jimmunol.1202448>.
37. Lang, P.A., Lang, K.S., Xu, H.C., Grusdat, M., Parish, I.A., Recher, M., Elfrod, A.R., Dhanji, S., Shaabani, N., Tran, C.W., et al. (2012). Natural killer cell activation enhances immune pathology and promotes chronic infection by limiting CD8 + T-cell immunity. *Proc. Natl. Acad. Sci. USA* **109**, 1210–1215. <https://doi.org/10.1073/pnas.1118834109>.
38. Waggoner, S.N., Cornberg, M., Selin, L.K., and Welsh, R.M. (2011). Natural killer cells act as rheostats modulating antiviral T cells. *Nature* **481**, 394–398. <https://doi.org/10.1038/nature10624>.
39. Pallmer, K., Barnstorf, I., Baumann, N.S., Borsa, M., Jonjic, S., and Oxenius, A. (2019). NK cells negatively regulate CD8 T cells via natural cytotoxicity receptor (NCR) 1 during LCMV infection. *PLoS Pathog.* **15**, e1007725. <https://doi.org/10.1371/journal.ppat.1007725>.
40. Wang, Y., Swiecki, M., Cella, M., Alber, G., Schreiber, R.D., Gilfillan, S., and Colonna, M. (2012). Timing and magnitude of type I interferon responses by distinct sensors impact CD8 T cell exhaustion and chronic viral infection. *Cell Host Microbe* **11**, 631–642. <https://doi.org/10.1016/j.chom.2012.05.003>.
41. Crouse, J., Bedenikovic, G., Wiesel, M., Ibberson, M., Xenarios, I., VonLaer, D., Kalinke, U., Vivier, E., Jonjic, S., and Oxenius, A. (2014). Type I Interferons Protect T Cells against NK Cell Attack Mediated by the Activating Receptor NCR1. *Immunity* **40**, 961–973. <https://doi.org/10.1016/j.immuni.2014.05.003>.
42. Srivastava, S., Koch, M.A., Pepper, M., and Campbell, D.J. (2014). Type I interferons directly inhibit regulatory T cells to allow optimal antiviral T cell responses during

- acute LCMV infection. *J. Exp. Med.* 211, 961–974. <https://doi.org/10.1084/jem.20131556>.
43. Zinkernagel, R.M., Pfau, C.J., Hengartner, H., and Althage, A. (1985). Susceptibility to murine lymphocytic choriomeningitis maps to class I MHC genes - A model for MHC/disease associations. *Nature* 316, 814–817. <https://doi.org/10.1038/316814a0>.
44. Christiaansen, A.F., Schmidt, M.E., Hartwig, S.M., and Varga, S.M. (2017). Host genetics play a critical role in controlling CD8 T cell function and lethal immunopathology during chronic viral infection. *PLoS Pathog.* 13, e1006498. <https://doi.org/10.1371/journal.ppat.1006498>.
45. Oldstone, M.B., Dixon, F.J., Mitchell, G.F., and McDevitt, H.O. (1973). Histocompatibility-linked genetic control of disease susceptibility. *J. Exp. Med.* 137, 1201–1212.
46. Chen, M.-H., Raffield, L.M., Mousas, A., Sakaue, S., Huffman, J.E., Moscati, A., Trivedi, B., Jiang, T., Akbari, P., Vuckovic, D., et al. (2020). Trans-ethnic and ancestry-specific blood-cell genetics in 746,667 individuals from 5 global populations. *Cell* 182, 1198–1213.e14. <https://doi.org/10.1016/j.cell.2020.06.045>.

STAR★METHODS

KEY RESOURCES TABLE

REAGENT or RESOURCE	SOURCE	IDENTIFIER
<i>Antibodies</i>		
Anti-mouse CD3, Purified, clone 145-2C11	Biolegend	Cat#100359; RRID:AB_2616673
Anti-mouse CD3, Af488, 17A2	Biolegend	Cat#100210; RRID:AB_389301
Anti-mouse CD3, BV421, 17A2	Biolegend	Cat#100335; RRID:AB_10898314
Anti-mouse CD4, APC, clone RM4-5	Biolegend	Cat#100516; RRID:AB_312719
Anti-mouse CD4, BV395, clone GK1.5	BD Sciences	Cat#563790; RRID:AB_2738426
Anti-mouse CD4, BV421, clone GK1.5	Biolegend	Cat#100443; RRID:AB_2562557
Anti-mouse CD4, FITC, clone GK1.5	Biolegend	Cat#100406; RRID: AB_312691
Anti-mouse CD4, PE, clone GK1.5	Biolegend	Cat#100408; RRID: AB_312693
Anti-mouse CD4, Purified, InVivoMab, clone GK1.5	BioXcell	Cat#BE0003-1; RRID: AB_1107636
Anti-mouse CD8a, APC, clone 53-6.7	Biolegend	Cat#100712; RRID: AB_312751
Anti-mouse CD8a, BV421, clone 53-6.7	BD Sciences	Cat#563898; RRID: AB_2738474
Anti-mouse CD8a, PE, clone 53-6.7	Biolegend	Cat#100707; RRID: AB_312746
Anti-mouse CD8, Purified, InVivoMab, 2.43	BioXCell	Cat#BE0061; RRID:AB_1125541
Anti-mouse CD11b, FITC, M170	Biolegend	Cat#101207; RRID:AB_312790
Anti-mouse CD11b, PE, M170	Biolegend	Cat#101205; RRID:AB_312788
Anti-mouse CD16/32; Purified; Clone 93	Biolegend	Cat#101320; RRID:AB_1574975
Anti-mouse CD28, Purified, clone 37.51	Biolegend	Cat#102121; RRID:AB_2810330
Anti-mouse CD44, Af700, clone IM7	Biolegend	Cat#103026; RRID:AB_493713
Anti-mouse CD44, FITC, clone IM7	Biolegend	Cat#103006; RRID: AB_312957
Anti-mouse CD44, PE, clone IM7	Biolegend	Cat#103006; RRID:AB_312957
Anti-mouse CD49a, PE-Cy7, clone HM α 1	Biolgend	Cat#142608; RRID:AB_2749931
Anti-mouse CD49b, APC, DX5	Biolegend	Cat#108909; RRID:AB_313416
Anti-mouse CD107a, FITC, clone 1D4B	Biolegend	Cat#121605; RRID: AB_572006
Anti-mouse CD107b, FITC, clone eBioABL-93	eBioscience	Cat#11-1072-81; RRID: AB_657579
Anti-mouse Cleaved Caspase3, Biotinylated, clone C292-605	BD biosciences	Cat#550557; RRID: AB_393750
Anti-mouse CXCR3, PE, clone CXCR3-173	Biolegend	Cat#126505; RRID:AB_2721669
Anti-mouse CXCR6, PE-Cy7, clone SA05101	Biolegend	Cat#151118; RRID:AB_2721669
Anti-mouse FoxP3, FITC, clone FJK-16s	Invitrogen	Cat#11-5773-82; RRID: AB_465243
Anti-mouse Granzyme B, AF647, clone GB11	Biolegend	Cat#515405; RRID: AB_2294995
Anti-mouse Granzyme-B, FITC, clone GB11	Biolegend	Cat#515403; RRID: AB_2114575
Anti-mouse Granzyme-B, Pacific Blue, clone GB11	Biolegend	Cat#515407; RRID:AB_2562195
Anti-mouse IFN γ , APC, clone XMG1.2	Biolegend	Cat#505810; RRID: AB_315404
Anti-mouse IFN γ , FITC, clone XMG1.2	Biolegend	Cat#505806; RRID: AB_315400
Anti-mouse IFN γ , Purified, clone XMG1.2	BioXCell	Cat#BE0055; RRID:AB_1107694
Anti-mouse IgG2a, purified, InVivoMab, C1.18.4	BioXCell	Cat#BE0085; RRID:AB_1107771
Anti-mouse IgG2bk, purified, InVivoMab, RMG2b-1	BioXCell	Cat#BE0086; RRID:AB_1107791
Anti-mouse IL-17a-PE, clone Tc11-18H10.1	Biolegend	Cat#506904; RRID:AB_315464

(Continued on next page)

Continued

REAGENT or RESOURCE	SOURCE	IDENTIFIER
Anti-mouse IL-4, Purified, clone 11B11	BioXCell	Cat#BE0045; RRID:AB_1107707
Anti-mouse NK1.1, Af700, clone PK136	Invitrogen	Cat#56-5941-82; RRID:AB_2574505
Anti-mouse NK1.1, PE, clone PK136	Biolegend	Cat#108707, RRID: AB_313394
Anti-mouse NK1.1, PerCP, clone PK136	Biolegend	Cat#108727; RRID:AB_2132706
Anti-mouse NK1.1, Purified, InVivoMab, clone PK136	BioXCell	Cat#BE0036; RRID:AB_1107737
Anti-mouse NKp46, BV421, clone 29414	Biolegend	Cat#137611; RRID:AB_10915472
Anti-mouse NKp46, PE, 29A1.4	Biolegend	Cat#137604; RRID:AB_2235755
Anti-mouse RORgt-APC, clone B20	eBioscience	Cat#17698182; RRID:AB_2573254
Anti-mouse Tbet-PE, clone 4B10	Biolegend	Cat#644810; RRID:AB_2200542
Bacterial and virus strains		
LCMV-Clone13	Whitmire lab	N/A, generated in house
Chemicals, peptides, and recombinant proteins		
ACK Lysing Buffer	Lonza	Cat#10-548E
Bovine Serum Albumin	Sigma-Aldrich	Cat#A4503
Brefeldin A Solution (1000X)	Biolegend	Cat#420601
Calcium chloride	Mallinckrodt Chem	Cat#4160-12
Collagenase Type IV	Gibco	Cat#17104-14-5
DMEM	Lonza	Cat#12-61F
EMEM	Sigma-Aldrich	Cat#56416C
FBS	GIBCO	Cat#26140-079
Ficoll	GE Healthcare	Cat#17-1440-02
Ghost Dye Red 780 Viability Dye	TONBO	Cat#13-0865-T100
GoTaq Green	Promega	Cat#M7122
HEPES	Lonza	Cat#17-737E
Ionomycin	Sigma Aldrich	Cat# I9657
L-glutamine	Lonza	Cat#17-605L
Magnesium chloride	Sigma Aldrich	Cat#M8266
Microtainer Blood Collection Tubes with K2EDTA	Becton Dickinson	Cat# 365974
MojoSort™ Buffer	Biolegend	Cat#480017
Monensin (1000X)	Biolegend	Cat#420701
Nonessential amino acids	Gibco	Cat#11140-050
OmniPur Ethidium Bromide	Calbiochem	Cat#18H235208
Penicillin-Streptomycin	Lonza BioWhittaker	Cat#BW17602E
Percoll	Cytiva	Cat#17089102
Pf23II restriction enzyme and buffer	ThermoFisher Scientific	Cat# FD0854
Phorbol 12-myristate 13-acetate	Sigma Aldrich	Cat#P8139
Proteinase K, recombinant, PCR grade	ThermoFisher Scientific	Cat#EO0491
Recombinant Human IL-2	Peptotech	Cat#200-02
Recombinant Human TGFb1	Peptotech	Cat#100-21
Recombinant Mouse IL-6	Biolegend	Cat# 575702
Recombinant Murine IL-12 p70	Peptotech	Cat# 210-12
RPMI 1640	Lonza	Cat#12-167F
Sodium chloride	VWR	Cat#7647-14-5

(Continued on next page)

Continued

REAGENT or RESOURCE	SOURCE	IDENTIFIER
Sodium Pyruvate	Lonza	Cat#13-115E
Taq DNA polymerase	Invitrogen	Cat#18038042
TBE Buffer, Molecular Biology Grade	Calbiochem	Cat#574795
Trizma hydrochloride	Sigma Aldrich	Cat#T5941-100G
Tween-20	Sigma-Aldrich	Cat# P1379
UltraPure Agarose	Invitrogen	Cat#16500
UltraPure™ 0.5M EDTA, pH 8.0	ThermoFisher Scientific	Cat#15575020
VspI (AseI) restriction enzyme and buffer	ThermoFisher Scientific	Cat# ER0911
Zombie Aqua Fixable Viability Dye	Biolegend	Cat#423101

Critical commercial assays

Foxp3 Permeabilization/Fixation kit	eBiosciences	Cat#421403
MojoSort Mouse CD4 T Cell Isolation Kit	Biolegend	Cat#480033
UltraComp eBeads™ Compensation beads	ThermoFisher Scientific	Cat#01-2222-41
Verikine Mouse IFN α ELISA	PBL Assay Science	Cat#42120-1

Experimental models: Cell lines

Vero-E6	Michael Buchmeier	The Scripps Research Institute, La Jolla, CA
BHK-21 cells	ATCC	Cat#CCL-10

Experimental models: Organisms/strains

Mouse: C57BL/6J	Jackson Laboratory (purchased during last 7 years, bred at UNC)	Cat#000664
Mouse: FVB/NJ	Jackson Laboratory (purchased during last 7 years, bred at UNC)	Cat#001800
Mouse: B6FVBF1	Backcrossed to B6/J in Whitmire lab	This work
Mouse: FVBB6F1	Backcrossed to B6/J in Whitmire lab	This work
Mouse: B6FVBN2	Backcrossed to B6/J in Whitmire lab	This work
Mouse: B6.FVB(17:30-55)25/JW	Backcrossed to B6/J in Whitmire la	This work
Mouse: B6.FVB(17:31-55)24/JW	Backcrossed to B6/J in Whitmire la	This work
Mouse: B6.FVB(17:35-55)20/JW	Backcrossed to B6/J in Whitmire la	This work

Oligonucleotides

Adgrf1-GENO FWD AAAGGGTTCCTGGAGTGTGC	Eurofins Genomics	This work
Adgrf1-GENO REV AGCTAACAGGACATCTCCAC	Eurofins Genomics	This work
Ubash3a-GENO FWD AGGCAATGGCTGGTGGATAC	Eurofins Genomics	This work
Ubash3a-GENO REV CTGTCTAGAGTCATCTGGAC	Eurofins Genomics	This work

Software and algorithms

FlowJo Software (10.8.1)	Tree Star	https://www.flowjo.com
Gene Ontology Browser	JAX	http://www.informatics.jax.org
GraphPad Prism (version 9.5.0)	GraphPad	https://www.graphpad.com
Human Mouse Homology Maps	NCBI	https://www.ncbi.nlm.nih.gov/projects/homology/maps/

(Continued on next page)

Continued

REAGENT or RESOURCE	SOURCE	IDENTIFIER
Mouse Genomes Project	Sanger	https://www.sanger.ac.uk/sanger/Mouse_SnpViewer/rel-1505
R/qrtl	Karl W. Broman et al. University of Wisconsin-Madison	https://qrtl.org/

RESOURCE AVAILABILITY

Lead contact

Further information and requests for resources and reagents should be directed to Jason Whitmire (jwhitmir@email.unc.edu).

Materials availability

All G6 mouse lines generated herein are available upon request. Transfers require standard institutional material transfer agreements and evidence of institutional (IACUC) approval.

Data and code availability

- All experimental data are available within this article. Data reported in this paper will be shared by the [lead contact](#) upon request.
- This paper does not report original code.
- Any additional information required to reanalyze the data reported in this paper is available from the [lead contact](#) upon request.

EXPERIMENTAL MODEL AND SUBJECT DETAILS

Mice

C57BL/6J (B6) mice were purchased from the Jackson Laboratory (Bar Harbor, Maine) during the period 2011–2019. FVB/N (FVB) were purchased from the Jackson Laboratory during the period 2019–2020. B6FVBF1 (F1) and B6 backcrossed lines, including N2, N3, etc., were bred at the University of North Carolina at Chapel Hill (UNC). All mice were bred and housed in a facility managed by the Division of Comparative Medicine at UNC in accordance with the policies and guidelines of the Institutional Animal Care and Use Committee (IACUC).

Breeding

FVB sires were iteratively bred to B6 dams over the course of five generations (F1, N2, N3, N4, N5, respectively) using a SNP marker-guided speed congenic design (PMID: 9178014 and 9049627). At the fifth generation (N5), mice heterozygous for the FVB-Chr17 QTL were bred together to produce heterozygous and homozygous offspring. Male and female offspring that were homozygous for the FVB-Chr17 QTL were bred together to generate a sixth generation congenic to B6 across the genome except for the FVB-Chr17 QTL. These sixth generation (G6) mice were maintained through inbreeding. During breeding, two N3 males were identified to have a meiotic recombination at the FVB-Chr17 QTL allele. These males were bred independently to generate three separate G6 lines, each named based on the size of the homozygous FVB-Chr17 QTL as determined by miniMUGA and PCR genotyping.

Full Inbred Line Identification

Referred to in this manuscript as:

B6.FVB(17:30-55)25/JW	G6_25
B6.FVB(17:31-55)24/JW	G6_24
B6.FVB(17:35-55)20/JW	G6_20

Virus

Mixed sex adult mice (8–10 weeks) received 2×10^6 plaque-forming units (PFU) LCMV-Clone13 by intravenous tail vein injection. Stocks of LCMV were produced from BHK-21 cells after infection with plaque-purified isolates and were negative for mycoplasma. Virus titer in serum, liver, lung, and kidney was quantified by plaque assay on Vero monolayers (PMID:6332167). Infected mice that approached a loss of > 20% initial starting body weight and/or had a body temperature recorded lower than 30°C were euthanized via isoflurane overdose. Weight and temperature measurements taken at the same time of day each day.

Cell culture

Vero cells (kidney epithelial; African green monkey; female) and BHK cells (fibroblasts; Syrian golden hamster; male) were propagated in DMEM supplemented with 5% heat-inactivated FBS, penicillin, and streptomycin.

METHOD DETAILS

Genotyping and quantitative trait locus (QTL) mapping

Mice were genotyped on the MiniMUGA array (<https://www.transnetyx.com/>) (PMID: 33067325). This array contains 10,819 genomic markers for mouse, with 2,999 diagnostic between FVB and C57BL6J (2969 across the X and autosome, 30 on the Y chromosome). Quantitative trait locus (QTL) mapping was performed with 63 N2 mice (28 male, 35 female). We used R/qtl (version 1.47.9) for the QTL mapping, with death by 8 dpi as a binary phenotype, sex as a covariate, and cross-type set to “bc” (backcross) (PMID: 35448524). Significance was determined by permuting the data 10,000 times and rerunning the association to generate a null distribution of the strongest LOD scores. We then set an empirical alpha < 0.05 threshold for our N2 analysis. The QTL interval was determined by a 1.5 LOD drop analysis using lodint(). Analyses were performed with R version. 4.0.4.

PCR genotyping

Tail DNA was isolated using a 1X digestion buffer (50mM Tris pH 8.8, 1mM EDTA, 0.5% Tween-20, 1:20 Proteinase K) incubated for 14 hours at 55°C. PCR amplification of DNA fragments (200-400 bp) was performed with the specific primers and Taq DNA polymerase. General PCR conditions were: 95°C, 5 minutes; [95°C for 30s; 72°C for 90s] x 35 cycles; 72°C for 5 minutes. Oligonucleotide primers for *Adgrf1* (F: AAAGGGTTCTGGAGTGTGC; R: AGCTAACAGGACATCTCCAC) and *Ubash3a* (F – AGGCAATGGCTGGTGGATAC; R - CTGTCTAGA GTCATCTGGAC) were custom-synthesized by Eurofins Genomics. PCR products were run on a 2% agarose gel and visualized by ethidium bromide staining. To distinguish between FVB and B6/J genotypes, *Ubash3a* PCR products were digested with Pf23II restriction enzyme and *Adgrf1* PCR products were digested with *VspI* (*AseI*) restriction enzyme prior to running the gel.

Variant analysis

FVB sequence (GCA_001624535.1) was compared to consensus C57BL/6J (GRCm39.p6) sequence for analyses. All non-synonymous variants and splice variants were selected within the Chr17:30–55Mb region. Variant Effect Predictor (VEP) (<http://useast.ensembl.org/Tools/VEP>) was used to identify the likely effect of each variant on exon splicing, gene expression, or protein sequence, as well as effects on putative intergenic regulatory regions. The effects of the variants were evaluated using the canonical transcript for each gene. Sorting Intolerant From Tolerant (SIFT) analysis software (https://useast.ensembl.org/Mus_musculus/Info/Index) predicted whether changes to coding sequence in FVB would impact protein structure or function. Highly significant changes were identified by either a SIFT score of < 0.05 and/or a VEP “Putative Impact Score” of high (McLaren et al., 2016). Immune-related genes were defined by the Gene Ontology Browser at the JAX database (<http://www.informatics.jax.org>), using the “Phenotypes, Alleles & Disease Models Search.”

Complete blood count (CBC) and alanine transferase (ALT)

Peripheral blood was analyzed on a Procyte Dx Hematology Analyzer (IDEXX Laboratories, Inc.) at the Animal Histopathology & Laboratory Medicine Core at UNC.

Histology

Tissues were harvested at necropsy and fixed in 10% neutral phosphate-buffered formalin for 36 hours and stored in 70% ethanol until processed for histology. Formalin-fixed paraffin-embedded tissues were sectioned at 5 μm thickness for histology. Sections were stained with hematoxylin and eosin (H&E) or anti-caspase-3 antibody according to the manufacturer’s protocol and examined for histological changes by light microscopy (an Olympus BX61 microscope) at UNC Microscopy Services Laboratory. All histological processes were conducted by Animal Histopathology Core Lab, Lineberger Comprehensive Cancer Center, UNC-CH.

In vivo depletions of cells

CD8⁺ and CD4⁺ T cells were depleted in mice using 250 μg anti-CD8 (clone 2.43) or 250 μg anti-CD4 (clone, GK1.5) given by intraperitoneal injection (i.p.) at days -1 and +3 post-infection. Control mice were given 250 μg non-depleting, isotype control antibody IgG2b,k. NK cells were depleted by giving mice 100 μg anti-NK1.1 (PK136) at days -2 and -3 post-infection. Control mice were given 100 μg non-depleting, isotype control antibody IgG2a.

Cell isolation and purification

Single-cell suspensions from spleens were prepared by physically disrupting the tissue over a 70 μm strainer. Erythrocytes were removed from the spleen suspension using ACK lysing buffer. Single-cell suspensions of liver were treated with Collagenase IV for 60 minutes and disrupted using a 70 μm strainer. Leukocytes were isolated from the liver suspension by mixing the cells with 45% Percoll, underlaying the cells with 80% Percoll, centrifuging, and isolating leukocytes from interphase. Blood leukocytes were isolated using heparinized capillary tubes and collected into 4% sodium citrate; cells were underlaid with Ficoll, centrifuged, and the leukocytes removed from the resulting interphase. All single-cell preparations were rinsed and re-suspended in 10% RPMI media.

Flow cytometry

Single cell suspensions of blood, spleen, and liver were stained directly *ex vivo* with fluorochrome-conjugated antibodies. Cell-surface staining was done in the presence of unlabeled antibodies against Fc-receptors. The intracellular staining was achieved using Foxp3 Permeabilization/Fixation kit. Antibody-stained cells were detected by FACSCalibur, LSRII, or LSR-Fortessa (BD Biosciences) cytometers. Data were analyzed using FlowJo software. Hierarchical gates were established by first assessing forward and side scatter size, discriminating live cells using a viability dye, discriminating singlets by comparing forward scatter height and width, and then resolving specific cell populations using isotypes, FMOs, and biological controls.

T cell degranulation

Single cell suspensions isolated from liver and spleen were stimulated with anti-CD3 (10 $\mu\text{g}/\text{mL}$, plate-bound) and anti-CD28 (1 $\mu\text{g}/\text{mL}$, soluble), or with LCMV peptides NP₁₁₈₋₁₂₆/GP₃₃₋₄₁ (1 $\mu\text{g}/\text{mL}$) in 10% RPMI and co-incubated with FITC-labeled anti-CD107a and anti-CD107b (1:50) for 3.5 hours at 37°C with 5-7% CO₂. 1X monensin was included after 1 hour of incubation. Unstimulated cells were used as controls.

NK cell degranulation

Single cell suspensions isolated from uninfected spleens were stimulated with PMA (40 ng/mL) and Ionomycin (2 μM) for 4 hours in the presence of FITC-labeled anti-CD107a and anti-CD107b (1:50) for 4 hours at 37°C with 5-7% CO₂. 1X monensin was included after 1 hour of incubation. Unstimulated cells were used as controls.

In vitro CD4 differentiation

CD4⁺ T cells from B6, FVB, or G6₂₄ were isolated using the magnetic bead enrichment Biogend mouse CD4 isolation kit according to the manufacturer's protocol. CD4⁺ T cells were stimulated with R10 media (RPMI 1640 with 10% FBS, 2 mM L-Glutamine, 100 IU/mL penicillin, 100 $\mu\text{g}/\text{mL}$ streptomycin, 1 x nonessential amino acids, 1 μM sodium pyruvate and 50 μM β -mercaptoethanol) with plate-bound 10 $\mu\text{g}/\text{mL}$ α -CD3e (clone 145C-11) and soluble 1 $\mu\text{g}/\text{mL}$ α -CD28 (clone 37.51). For T regulatory conditions, cells were cultured with 2.5 ng/mL rhTGF β 1 (Pepro- tech) and 50 U/mL of IL-2. For Th1, cells were cultured with 10 ng/mL IL-12 and 10 $\mu\text{g}/\text{mL}$ α -IL4 (11B11).

CD4 subset stimulation and staining

A viability dye (Ghost Red780) was applied to exclude dead cells. Intracellular staining for Foxp3 (clone FJK-16S), Tbet (clone 4B10), IFN γ (clone XMG1.2), ROR γ t (clone B20), and IL-17A (clone TC11-18H10.1) was performed using the Foxp3 Permeabilization/Fixation kit (eBioscience). To measure cytokine production (IFN γ and IL-17A), cells were restimulated with PMA (40 ng/mL) and Ionomycin (2 μM) for 4 hours in the presence of Brefeldin A for four hours at 37°C. Samples were acquired using a LSRII or LSR-Fortessa and data was analyzed with FlowJo version 10 (Tree Star).

QUANTIFICATION AND STATISTICAL ANALYSIS

Parametric tests were conducted using unpaired two-tailed Student's t-test for two groups or one-way analysis of variance (ANOVA) with Bonferroni multiple comparison test for more than two groups. When data were not normally distributed, non-parametric tests were used (Mann-Whitney U test for two groups, Kruskal-Wallis with Dunn's multiple comparison test for more than two groups). Where applicable, a Grubbs' test or ESD (extreme studentized deviate) was performed to identify outliers in data sets. Statistical analyses and graphing were done with Prism software (GraphPad Software Inc.). P values considered significant are indicated in figure legends as * $p < 0.05$; ** $p < 0.001$; *** $p < 0.0001$, **** $p < 0.00001$, ***** $p < 0.000001$; ns (not significant) = $p > 0.05$. All data are presented as mean \pm SD values.